6-11

SANDIA REPORT

SAND96-1309 • UC-706
Unlimited Release
Printed June 1996

Rapid Prototype and Test

D. L. Gregory, B. D. Hansche

Prepared by
Sandia National Laboratories
Albuquerque, New Mexico 87185 and Livermore, California 94550
for the United States Department of Energy
under Contract DE-AC04-94AL85000

Approved for public release; distribution is unlimited.

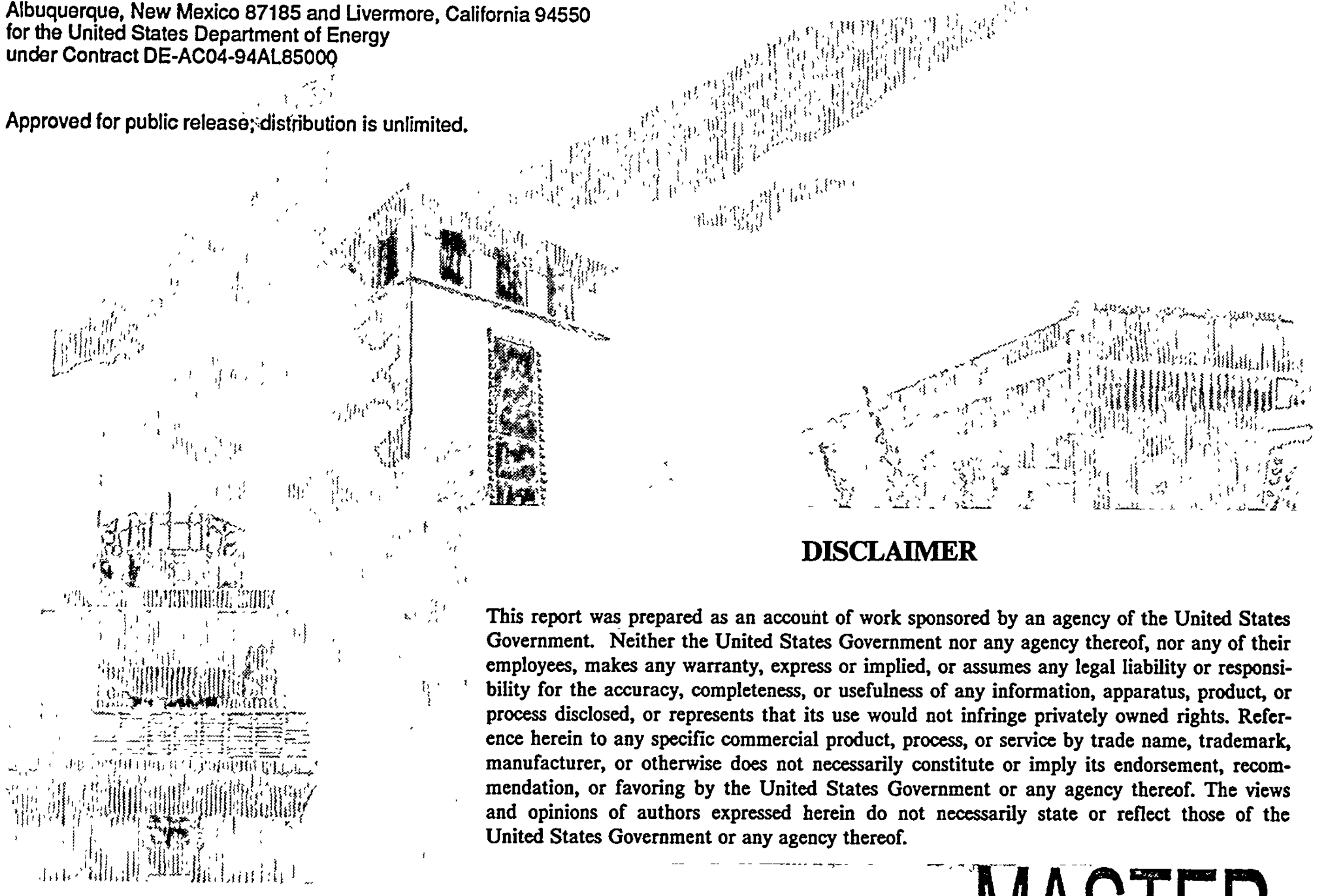

DISCLAIMER

This report was prepared as an account of work sponsored by an agency of the United States Government. Neither the United States Government nor any agency thereof, nor any of their employees, makes any warranty, express or implied, or assumes any legal liability or responsibility for the accuracy, completeness, or usefulness of any information, apparatus, product, or process disclosed, or represents that its use would not infringe privately owned rights. Reference herein to any specific commercial product, process, or service by trade name, trademark, manufacturer, or otherwise does not necessarily constitute or imply its endorsement, recommendation, or favoring by the United States Government or any agency thereof. The views and opinions of authors expressed herein do not necessarily state or reflect those of the United States Government or any agency thereof.

SF2900Q(8-81)

DISTRIBUTION OF THIS DOCUMENT IS UNLIMITED

MASTER

Issued by Sandia National Laboratories, operated for the United States Department of Energy by Sandia Corporation.

NOTICE: This report was prepared as an account of work sponsored by an agency of the United States Government. Neither the United States Government nor any agency thereof, nor any of their employees, nor any of their contractors, subcontractors, or their employees, makes any warranty, express or implied, or assumes any legal liability or responsibility for the accuracy, completeness, or usefulness of any information, apparatus, product, or process disclosed, or represents that its use would not infringe privately owned rights. Reference herein to any specific commercial product, process, or service by trade name, trademark, manufacturer, or otherwise, does not necessarily constitute or imply its endorsement, recommendation, or favoring by the United States Government, any agency thereof or any of their contractors or subcontractors. The views and opinions expressed herein do not necessarily state or reflect those of the United States Government, any agency thereof or any of their contractors.

Printed in the United States of America. This report has been reproduced directly from the best available copy.

Available to DOE and DOE contractors from
Office of Scientific and Technical Information
PO Box 62
Oak Ridge, TN 37831

Prices available from (615) 576-8401, FTS 626-8401

Available to the public from
National Technical Information Service
US Department of Commerce
5285 Port Royal Rd
Springfield, VA 22161

NTIS price codes
Printed copy: A05
Microfiche copy: A01

SAND96-1309
Unlimited Release
Printed June 1996

Distribution
Category UC-706

Rapid Prototype and Test

D. L. Gregory and B. D. Hansche
Manufacturing and Rapid Prototype Testing Department
Sandia National Laboratories
Albuquerque, NM 87185

Abstract

In order to support advanced manufacturing, Sandia has acquired the capability to produce plastic prototypes using stereolithography. Currently, these prototypes are used mainly to verify part geometry and "fit and form" checks. This project investigates methods for rapidly testing these plastic prototypes, and inferring from prototype test data actual metal part performance and behavior. Performances examined include static load/stress response, and structural dynamic (modal) and vibration behavior. The integration of advanced non-contacting measurement techniques including scanning laser velocimetry, laser holography, and thermoelasticity into testing of these prototypes is described. Photoelastic properties of the epoxy prototypes to reveal full field stress/strain fields are also explored.

Acknowledgments

The authors would like to thank several other contributors in this effort. Garth M. Reese of the Structural Dynamics and Vibration Control Department for his development of finite element models to support the project. Clinton Atwood, Brian Pardo, and Daryl Ruckaway of the Rapid Prototyping Department for the excellent support in developing the prototypes and other model hardware; Marlene Shields for her innovative work in the structures laboratory testing the prototypes; and Tom Togami for his photoelastic measurements.

Contents

Figures

Tables

This Page Left Intentionally Blank

Chapter 1

Rapid Prototype and Test

Introduction

The recently developed stereolithography process[1] has shown great potential for reducing the time between concept and product realization. The stereolithography process has provided the means of economically generating very exact plastic prototype parts from three dimensional solid models. These prototypes are currently used primarily to verify geometries, for interference checks, and for product visualization. The ability to perform mechanical tests on these plastic prototypes and infer actual metal part structural performance could have a significant impact on the design cycle to bring a product to market. These results could also be used to validate analytical models early in the design process to provide predictive models for effective design iterations and tradeoff studies.

This report describes the results of a Laboratory Directed Research and Development (LDRD) study to perform mechanical tests on plastic prototype parts and develop techniques to predict the performance of actual metal parts. These performances include static load/stress, structural dynamic (modal) and vibrational behavior. A second objective of the study was to integrate new full field measurement techniques to provide rapid, spatially dense structural measurements to aid the designer and obtain enhanced information for analytical model validation. The rest of this chapter gives a brief description of these measurement techniques and technologies.

Background

The use of plastic models to predict the structural behavior of actual metal parts or assemblies is not a new concept [2,3,4]. The successful use of plastic parts to uncover design problems is well documented. Often the plastic models were scaled models of much larger complicated structures for which the costs of construction were prohibitive in the early design stages. In the past, the cost and time required for creating these models with sufficient detail was significant. Plastic models required the machining or casting of molds and further detailed machining operations. These machining operations were required to include features such as bolt holes, fillets, and other details to provide sufficient fidelity of these models to allow accurate predictions of the structural behavior of actual metal parts. A trade-off of cost to accuracy was always a concern with the traditional techniques of creating plastic models.

The development of the stereolithography process has enabled engineers to rapidly produce prototype plastic parts with astounding accuracy including bolt holes, countersinks, fillets, cutouts, etc. These stereolithography plastic prototypes include all the detail and are nearly perfect replicas of the actual parts. They afford detail that cannot be included in finite element models. These very exact plastic prototypes are produced rapidly without expensive tooling and machining operations and offer a new realm of opportunity for the use of plastic models to predict the structural performance of actual metal parts.

Stereolithography Process

An excellent discussion of the stereolithography process is given in Reference [1]. To briefly summarize, the process to produce these very accurate prototypes utilizes special photoreactive plastic resins selectively cured with a computer controlled laser system. A 3-D solid model from a Computer Aided Design (CAD) file or by some other means is used to create a file which is essentially the geometry of the part in a series of very thin parallel slices. The computer uses this file to guide the laser in various patterns to generate the plastic prototype part. Each slice is built on top of the previous slices to create a 3D model. Different patterns of the laser are used to optimize the build to minimize internal stresses due to the curing process which can create dimensional warping of the part. Other patterns are developed to provide prototype parts which can be used directly in an investment casting process (Quick-Cast^{TM}). The tolerances achieved vary with materials, but with the epoxy resins the tolerances in the slice plane are on the order of .005 inches and somewhat greater for the out of plane dimensions. All of the plastic parts examined in this study were fabricated using the ACES^{TM} build style to furnish solid prototype plastic parts. The parts were post cured in an ultra-violet oven to insure that the complete part is fully cured. A curing time of one hour was requested for all of the parts used in this study. In addition, several metal bicycle cranks were made by the Quick-Cast process.

Prototype parts used in this study were fabricated using the SLA 250 machine with working dimensions of 10" x 10" x 10", and the SLA 500 machine with working dimensions of 20" x 20" x 28". These systems were manufactured by 3-D Systems Incorporated.

Wide Area Non-contact Measurements

One of the stated goals of the Rapid Prototype Test LDRD was to apply wide area non-contact measurements to the test objects. There are several motivations for this aspect of the program. One of the current development areas in testing technology is model validation, or correlation of measurement results with finite element (FE) models. Traditionally, this has been done with single point transducer data, correlating perhaps tens or hundreds of measurements with the tens of thousands of degrees of freedom of the model. Development of improved correlation techniques requires improved measurement techniques, providing hundreds or thousands of data points to better match the resolution of the model. This requires wide area, or "imaging" measurement techniques. Most of these are non-contact due to the impracticality of attaching that many physical sensors to the model. Another motivation for using non-contact sensing in this particular project is the mass-loading effect of the physical sensors. Since the density of the rapid prototype epoxy is lower than metals, the relative mass of the sensors is higher for these parts than for the corresponding metal parts. This makes the mass-loading error more severe, even for a few sensors, as demonstrated in several examples later in this report.

There are many non-contact measurement techniques available, in various stages of maturity. These can be categorized as <u>point</u> techniques, where measurements are made at a single point at a time, and that measurement location is scanned over the part to build up an array of data (image), and <u>area or imaging</u> techniques where an array of data points is taken in parallel, as with a video camera. Some of these techniques which were not used in this study, but which should be mentioned for completeness, are acoustic, microwave, and LIDAR measurements. Acoustic measurements such as ultrasonic pulse echo (usually a point technique) typically require the part to be immersed in a dense fluid such as water. Acoustic measurements are sensitive to density variations as well as surface position, and are one of the few true 3D techniques, being able to scan into the volume of the part, as opposed to seeing only the outer surface. Microwave measurements require a conductive surface to sense, so are typically not applicable to epoxy parts. LIDAR, or light based radar, has a typical distance resolution of a few mm, and might be useful for large deformation tests such as crush or impact tests.

Position and Deformation Measurement

Sensitivity vectors: Most of the optical position or displacement measurement techniques measure a <u>scalar</u> quantity at each measurement point, which is the projection of the actual position or displacement onto a <u>sensitivity vector</u>. This vector depends on the type of technique and geometry of the sensors. It defines the direction sensitivity of a particular measurement. Measurement of three dimensional vector information requires at least three independent measurements for each data point.

Optical position or deformation measurement techniques can be categorized as "coherent" or "incoherent". The incoherent techniques include standard "machine vision". These techniques measure lateral motion of the image on a two dimensional sensor such as a CCD camera. Stereo or triangulation techniques can be used to get sensitivity vectors normal to the plane of the sample. Incoherent optical techniques can be further subdivided into active or "structured light" techniques where the object is illuminated with a known pattern, and passive techniques where the only pattern to track is the image of the object itself. There are both point and imaging implementations of these techniques, and in general the field is mature, driven by machine vision and surveillance customers.

Point Triangulation techniques typically use active illumination, where the object is illuminated by a laser beam, and the image of the illumination spot is viewed at an angle. The motion sensitivity vector is approximately in the direction from the measurement point toward the instrument. Fixed (non-scanning) sensors are cheap and fast, with resolutions from sub-micron to cm, but measure only one point. In applications requiring high resolution and tolerating slow speeds, they are mechanically scanned. There are several commercial systems based on scanning point triangulation.

Imaging Triangulation techniques include active and passive embodiments. Moiré techniques can be included in this category[5]. In general, if a pattern of light is projected on an object ("active" illumination), the sensitivity vector tends to be in the direction of the instrument (out-of-plane motion), while if the pattern is painted on the object, or if the object structure itself is tracked ("passive"), the sensitivity vector tends to be in the plane of the sample. These techniques can be implemented with either video or high speed film imaging systems, and hence can be applied to dynamic events. Resolutions vary widely depending on implementation--deformation resolutions of a few microns have been demonstrated with passive systems.

Coherent Optical Techniques measure the phase of coherent light scattered from the object. They typically have deformation resolutions of a fraction of a micron, with an upper range of tens to hundreds of microns. Electronic speckle pattern interferometry and laser Doppler interferometry, both coherent techniques, were used in this project.

Holographic Interferometry (Holometry) and Electronic Speckle Pattern Interferometry (ESPI) are imaging techniques that measure deformation, or relative motion of the surface of a part[6,7]. They are quite similar, with holometry using film and ESPI electronic imaging. The key to their operation is that the <u>phase</u> of the light forming the image of the part is recorded (by use of an internal reference beam). In <u>static</u> holometry or ESPI, an image of the part is recorded. The part is then stressed by heating, mechanical loading, etc. which causes motion of the part. After the stress is applied, another image is recorded, and the two images are compared interferometrically as indicated in Figure 1.1. Each image point is a separate interference experiment, with the intensity at that point proportional to the cosine of the optical path difference in wavelengths:

$$I = I_0 + I_f \cos(\mathbf{k} \bullet \mathbf{d}) \qquad (1.1)$$

where the sensitivity vector

$$\mathbf{k} = (2\pi/\lambda)\,(\mathbf{k}_0 - \mathbf{k}_i) \qquad (1.2)$$

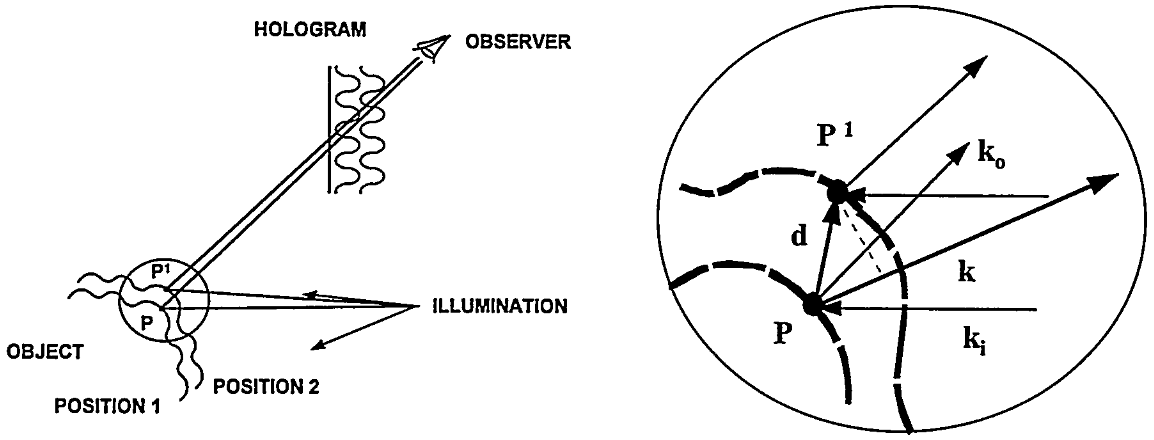

Figure 1.1. Holographic interferometry. **k** is sensitivity vector = $\mathbf{k}_o - \mathbf{k}_i$, where $\mathbf{k}_i$ and $\mathbf{k}_o$ are illumination and observation unit vectors, and **d** is displacement vector. Total optical path length change is $\lambda(\mathbf{d} \bullet \mathbf{k})$.

bisects the angle formed by the illumination and viewing directions which are defined by unit vectors $\mathbf{k}_0$ and $\mathbf{k}_i$. If the motion of a point results in a total optical path change of an integral number of wavelengths, the two images interfere constructively, and the point is bright. If the motion results in an optical path change of an integral plus half wavelength, the images interfere destructively, and the point is dark. Thus the image appears covered with bright and dark fringes (for example, see Figure 4.17), where each bright fringe represents a difference of one wavelength in optical path change. Typically, the illumination and viewing directions are both nearly perpendicular to the part surface (hence, so is the sensitivity vector), and the fringes can be interpreted as displacement contours of half a wavelength, or about 0.26 micron for the 0.53 micron wavelength light used in the ESPI instrument used for this project. Note that these are displacement contours, not surface shape contours.

Holometry and ESPI can also be applied in a time average mode, where an image is integrated over many cycles of a vibrational deformation, rather than being the result of interfering before-after images as above. The intensity at each image point is the integral of the instantaneous cosine fringe pattern described above, which results in a Bessel function. Areas where there is no motion--the node lines--appear fully bright. All other areas are dimmer, but the Bessel fringes still contain quantitative deformation information. Similar to the contours of displacement described above, each fringe represents a peak-to-peak vibration amplitude of about 0.26 microns. This technique is useful for rapid visualization of vibrational operating shapes. Note that for structures with low damping (high Q), these operating shapes are essentially identical to the mode shapes, which are mathematical entities used to represent a decomposition of a particular structure's dynamic response. Structures with high damping, like the epoxies used in rapid prototyping, tend to vibrate in an operating shape composed of the superposition of several nearby modes.

Since the quantity measured is essentially the changes in distance to the sensor, common mode noise in the form of instrument vibration and rigid body motion of the object can often swamp the measurement. Techniques to minimize or eliminate these effects are developmental. Qualitative holometry and ESPI are mature techniques--the Nondestructive Testing (NDT) group at Sandia has been doing holometry for 20 years, and has had a commercial ESPI system for several years. Quantitative, full 3D analysis is still developmental--the commercial system owned by the NDT group is supposedly capable of 3D analysis, but there are limitations. The examples in this project all have the system arranged so the sensitivity vector is essentially perpendicular to the object surface, and the images are displacement or vibration amplitude contour maps, with a contour interval of one half wavelength or about 0.26 microns.

The COBRA simulation code is a virtual testing program which is designed to simulate the action of holometry, ESPI and shearography. It was written over the last few years by Sandia and New Mexico State University personnel, funded mainly by the Federal Aviation Administration. The user describes the optical geometry of the system. The geometry and deformation information describing the test part can be generated deterministically (for simple objects), or input via finite element model results. The program predicts the fringe pattern that should be generated by the test. The main objective for writing this program was to facilitate and optimize use of these coherent optics techniques--to answer the question, "given a particular object and deformation, what technique and optical setup will be most effective in detecting the deformation?". In this study, COBRA was used to model the deformation of some of the test parts, as a means to correlate the experimental data with finite element predictions. Ideally, the coherent optical data would be analyzed for 3D deformation, and the correlation done in the domain of part deformation. This capability is not generally available yet, and development of 3D analysis techniques is ongoing.

Laser Doppler Velocimetry (LDV) is a point technique which measures the frequency shift instead of the absolute phase of the scattered light[8]. The fundamental quantity measured is surface velocity as projected on the sensitivity vector, which is in the direction of the instrument for all the measurements in this project. Commercial instruments typically have a velocity range of a few tenths of a mm per second to one meter per second, using several discrete gain settings. The instrument used in this study takes several seconds to acquire information for each physical location. While this instrument can be used to build up images by scanning multiple measurement points, this can take several hours. For this project, the LDV was used in the same way accelerometers are typically used, taking broadband frequency-response-function (FRF) data at a few locations on the object.

Thermoelastic Imaging

Thermoelastic imaging relies on the thermoelastic effect: within the elastic range, the temperature of a material changes slightly when stress is applied[9]. This temperature change is reversible, and proportional to the sum of the principal stresses via the material dependent <u>thermoelastic constant</u>. These temperature changes are typically a few microdegrees K, so a synchronous technique is necessary to detect them. There are currently two commercial thermoelastic imaging systems available, one a scanned point device (SPATE, by Ometron), and one an imaging array device (Deltatherm, by Stress Photonics).

Photoelastic Properties

One of the most interesting discoveries during this study is that the Ciba-Geigi Epoxy 5170 and 5180 resins yield prototype parts which have photoelastic properties. It should be noted that these are not the only plastic resins used in the stereolithography process, but were the ones available for study during this project. Photoelastic properties allow the full field strain and stress patterns of a part to be deduced through the analysis of fringe patterns using a polarized light source and an appropriate analyzer. The stresses and strains in two dimensional parts, fabricated with the stereolithography process, can be examined directly using classical photoelastic measurement techniques. Three dimensional parts can be analyzed using “frozen stress” techniques where three dimensional stresses developed under loading are locked into the parts during a freezing cycle and the stresses analyzed from thin slices cut through the cross section of the parts after the freezing cycle. These stress measurement techniques are discussed later in the report.

Chapter 2

Material Characterization

The nature of the stereolithography process requires that layers of material be selectively cured and sequentially added to the build to produce the prototype part. This layering effect leads to questions regarding the mechanical properties of the prototypes including isotropy and elastic moduli. The plastic materials are viscoelastic and consequently, have elastic moduli which are functions of frequency which complicates the scaling of plastic prototype dynamic behavior to the actual metal parts. The moduli of the plastic parts will monotonically increase with frequency since these materials are strain rate dependent. These properties are critical to the accurate scaling of the plastic prototype parts mechanical behavior to that of the actual metal parts. A number of experiments were performed to characterize the mechanical properties of the materials.

At the time of the start of this study there were essentially three photosensitive resins available at Sandia to evaluate. These were the Ciba Geigy 5170 and 5180 Epoxies and the Ciba Geigy 5154 Acrylic resin.

Isotropy

Isotropic material properties such as those found for homogeneous metal parts means that the density and elastic moduli are the same in all directions. The discovery of anisotropic material properties in the plastic prototypes would cause the scaling of mechanical behavior to metal parts to be essentially untractable. Acoustic velocity tests using a non-contacting ultrasonic technique were performed to directly measure Young's modulus, bulk modulus, shear modulus, and Poisson's ratio. A total of eleven rectangular parallpiped material samples were fabricated using the stereolithography process to allow the elastic constants to be determined parallel and orthogonal to the material lay-up. The nominal dimensions of the material samples were 0.5 x 0.6 x 0.7 inches. The ultrasound technique involves inducing elastic compression and shear waves into the material specimens and computing the wave speeds in the different directions. The wavelengths of the acoustic waves (2.25 MHz) were sufficiently small to resolve differences due to the material layering such as voids between layers which might not be resolved using other low frequency techniques such as standard tensile testing. The results are summarized in Table 2.1. The X and Y axis results are in the plane of the lay-up and the Z axis results are normal to the material lay-up. The reported values are the average of the eleven material specimens with very little scatter in the measurements. The results show that no significant directional differences exist between the elastic constants and the material can be treated as isotropic. It should be noted that these elastic constants were derived at very high frequency (2.25 MHz) to investigate any anisotropic behavior due to the layering effects. These elastic constants are not representative of the material properties at lower frequencies since the elastic moduli are functions of frequency for plastic materials. The frequency dependence of the elastic moduli are discussed later in the report.

Direction	Bulk Modulus (MPSI)	Young's Modulus (MPSI)	Shear Modulus (MPSI)	Poisson's Ratio	Lame Constant (MPSI)
X	.768	.562	.204	.378	.633
Y	.762	.561	.203	.378	.626
Z	.760	.561	.204	.377	.625

Table 2.1 Isotropy evaluation of 5170 epoxy

Static Tensile Tests

A series of standard tensile tests were performed on "dog bone" tensile specimens directly produced with the stereolithography process with the 5170 and 5180 Epoxy resins and the 5154 Acrylic resin. The tensile specimens are shown in Figure 2.1. These tests were performed on multiple specimens of each resin at three different strain rates to investigate the strain rate dependence of each material. Measurements included Young's modulus, peak stress, strain at peak, and stress at 0.2% yield. Young's moduli were determined from the secant modulus at the maximum slope (approximately 0.5% strain).

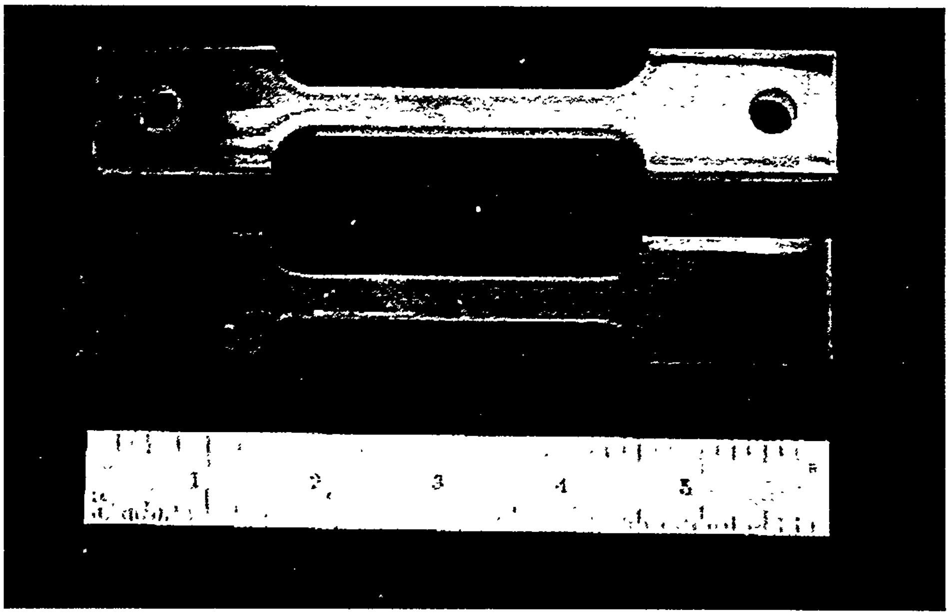

Figure 2.1 Tensile specimens for elastic modulus and photoelastic stress-optic coefficient

5154 Acrylic Resin tensile test results are shown in Figure 2.2. The plot in Figure 2.2 shows the strain rate dependence of the acrylic resin. The average Young's modulus and other material characteristics are listed in Table 2.2. The specimens fabricated from the acrylic resin demonstrated out-of-plane warping which increased with time. *This result eliminated the acrylic resins from further consideration for this study.*

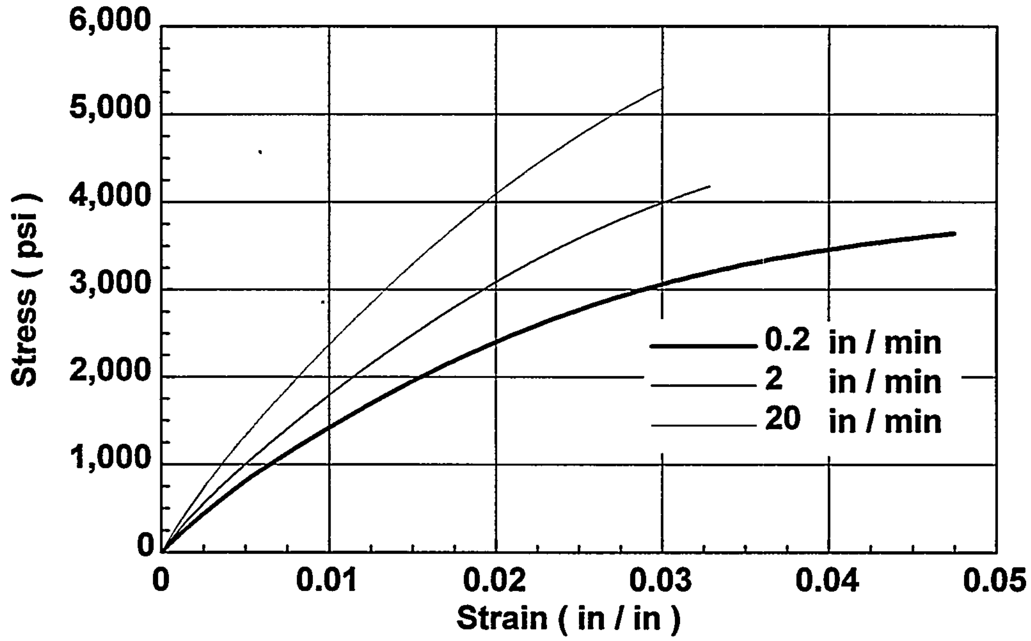

Figure 2.2 5154 acrylic resin tensile test results

Cross-Head Speed (in/min)	Young's Modulus (*E*) (ksi)	Stress at Peak (Break for Acrylic) (psi)	Stress at 0.2% Yield (psi)	Percent Strain at Peak (%)
0.2	170.9	3541	1541	4.4
2.0	214.5	4044	1961	3.5
20.0	280.3	5368	2514	3.2

Table 2.2 5154 acrylic tensile test results

5170 and 5180 Epoxy Resin tensile test results are summarized below. The 5170 Epoxy resin samples are shown in Figure 2.3 with the tabulation of results listed in Table 2.3. Similar results for the 5180 Epoxy resin is shown in Figure 2.4 and Table 2.4. The elastic modulus for the epoxy resins are greater than twice that of the acrylic resin. The SLA 250 machine utilized the 5170 epoxy and the SLA 500 machine used 5180 epoxy for purposes of this study. Both of the epoxy resins demonstrated similar mechanical properties and were much superior to the 5451 acrylic resin for dimensional stability. The requested cross-head speeds of 2.0 and 20.0 inches per minute could not be achieved with the tensile test machine due to the higher stiffness of the epoxy resins and the limited force capability of the tensile machine. The requested cross-head speeds and the actual strain rates that were achieved are given in Tables 2.3 and 2.4. The plots reflect the requested cross-head speed.

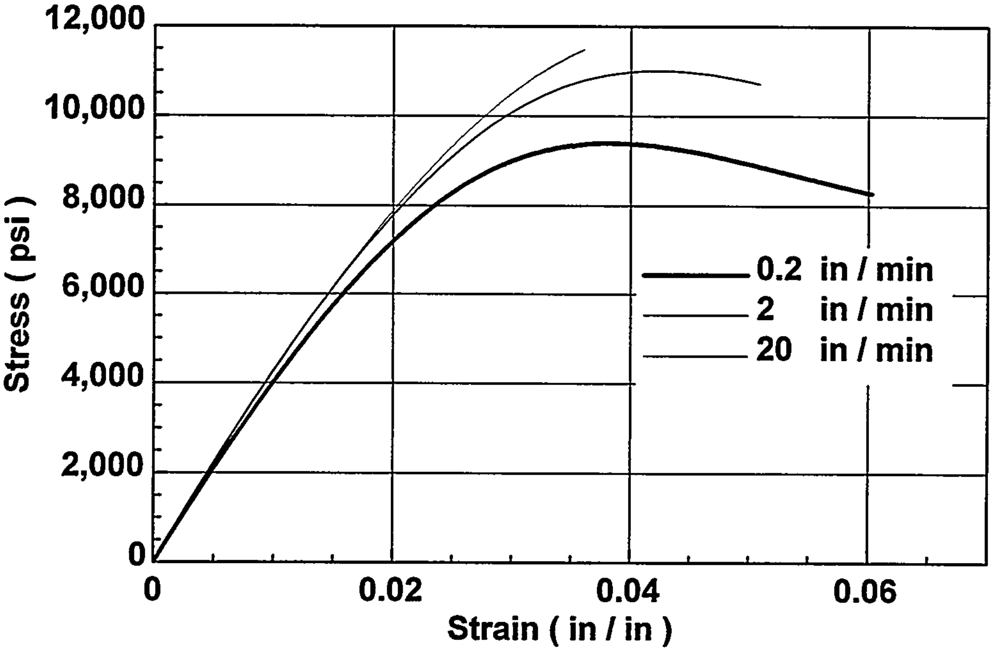

Figure 2.3 5170 epoxy tensile test results

Requested Cross-Head Speed (in/min)	Actual Strain Rate (sec^{-1})	Young's Modulus (*E*) (ksi)	Stress at Peak (psi)	Stress at 0.2% Yield (psi)	Strain at Peak (%)
0.2	4.0E-4	424.4	9460	6358	3.86
2.0	4.0E-3	444.8	11,080	7233	4.23
20.0	5.0E-2	443.7	11,585	7478	3.83

Table 2.3 5170 epoxy tensile test results

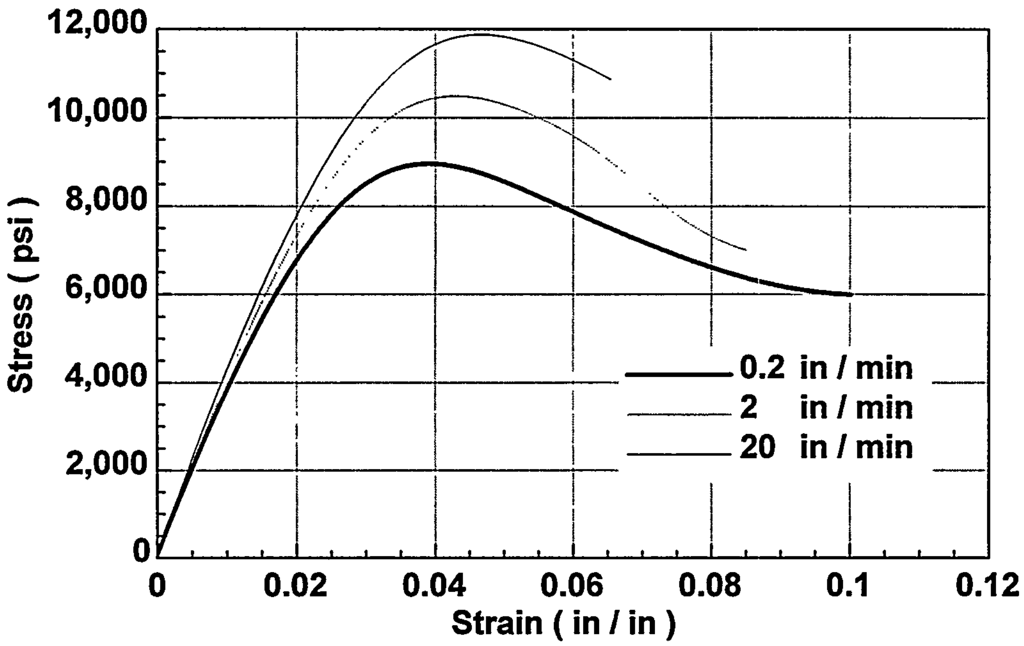

Figure 2.4 5180 epoxy tensile test results

Requested Cross-Head Speed (in/min)	Actual Strain Rate (sec^{-1})	Young's Modulus (E) (ksi)	Stress at Peak (psi)	Stress at 0.2% Yield (psi)	Percent Strain at Peak (%)
0.2	5.5E-4	408.8	9031	5612	3.91
2.0	6.4E-3	433.4	10,500	6409	4.24
20.0	5.7E-2	447.0	11,880	7091	4.66

Table 2.4. 5180 epoxy tensile test results

Dynamic Modulus Characterization

A series of experiments were performed to determine the frequency dependence of the elastic modulus of the 5180 epoxy resins. The plastic resins used in the stereolithography process exhibit similar behavior to other plastic materials in that they are viscoelastic and exhibit strain rate dependence [3,10] which creates a frequency dependence (strain rate) on the elastic modulus. As will be discussed later, the scaling of vibrational frequencies of plastic prototype parts requires knowledge of the elastic modulus as a function of frequency.

Beams of various lengths were fabricated with the stereolithography process to give a spectrum of natural frequencies over a large bandwidth. The beams were tested in a free-free boundary condition in the axial direction and a fixed-free (cantilevered) boundary condition in the lateral direction using impact excitation with a small instrumented hammer. The dynamic response of the beams to the excitation was measured with a small accelerometer through the use of a digital signal analyzer. The frequencies were measured and used with the theoretical frequency equation for the beams to calculate the elastic modulus at each natural frequency and these results were plotted to create a plot of the modulus as a function of frequency. The theoretical frequency equation from Reference [11] for the axial modes of a free-free beam is given as:

$$f_n = \frac{n}{2l}\sqrt{\frac{Eg}{\gamma}} \tag{2.1}$$

solving for the elastic modulus E:

$$E_n = \frac{4\gamma l^2}{g}\left(\frac{f_n}{n}\right)^2 \tag{2.2}$$

where:

E_n = Young's Modulus at the n$^{\text{th}}$ natural frequency, psi
g = acceleration of gravity, in/sec^2
γ = specific weight, lb/in^3
l = length of beam, in
n = mode number (1,2,3,....)

The theoretical frequency equation [11] of an Euler-Bernoulli cantilevered beam is:

$$f_n = \frac{K_n^2}{2\pi}\sqrt{\frac{EIg}{A\gamma}} \tag{2.3}$$

Solving for the elastic modulus, *E:*

$$E_n = \left[\frac{4\pi^2 A\gamma}{Ig}\right]\left(\frac{f_n}{K_n^2}\right)^2 \tag{2.4}$$

where:

E_n = Young's modulus at the n$^{\text{th}}$ natural frequency, psi
f_n = natural frequency, Hz
A = cross sectional area, in^2
I = area moment of inertia, in^4
g = acceleration of gravity, in/sec^2

γ = specific weight, lb/in^3
K_n = constant determined from frequency equation per Table 5.
n = subscript denoting the nth natural frequency

$K_1 l$	$K_2 l$	$K_3 l$	$K_4 l$	$K_5 l$	$K_6 l$
1.8751041	4.6940911	7.8547574	10.9955407	14.1371684	17.278760

Table 2.5 Roots of frequency equation for rectangular cantilevered beam

The lengths of the beams are limited by the working dimensions of the stereolithography machines. The length dimensions directly effect the frequencies that can be realized for the determination of the elastic modulus of the plastic prototype materials. In the use of the axial frequency equation the only physical dimension of the beam of concern is the length and errors in the width and thickness unless very gross are not of concern. Beams fabricated with 5180 epoxy were fabricated with dimensions of 18.0 inch x 1.0 inch x 0.25 inch for these experiments. In the axial direction, measurements were made with the length of the beams changed in 1.0 inch increments by cutting the beams after each measurement to the minimum length of 12.0 inches spanning the frequency range of 1800 to 6000 Hz.

To investigate frequencies below this range an 18.0 inch beam was configured and tested in a cantilevered boundary condition with a 17.0 inch effective length to give frequencies ranging from 10 to 850 Hz. The computed elastic modulus from the measured frequencies, as shown in Equation (2.4) is very sensitive to the physical dimensions of the beams. The thickness, *t*, is cubed in the calculation and the length is involved in the calculation of K_n, which is to the 4th power. Therefore, special attention must be made in measuring the effective cantilevered length and the specimen thickness used for the experiment. Furthermore, the given frequency equation does not include rotary inertia or shear deformation effects. To minimize errors due to these effects the thickness to length ratio of the calibration beams should be at least 20:1. The accelerometer used to measure the frequencies will also mass-load the beams creating additional errors. A light weight accelerometer mounted close to the clamped end should be used to minimize the mass-loading. A non-contacting measurement such as a laser Doppler velocimeter could be used to eliminate the mass loading effect though it was not used in this study. The effect of the rotary inertia, shear deformation, and mass-loading will be to lower the measured epoxy beam frequencies which will cause the calculated dynamic modulus to be *less* than the actual modulus.

The results, given in Figure 2.5, show that the elastic modulus monotonically increases with frequency. The slope of the curve is relatively small above approximately 1000 Hz and only small errors are incurred by using a nominal value over a fairly large range of frequencies. Detailed measurements of the elastic modulus as a function of frequency are required for very accurate scaling if the application so demands.

The material properties of the plastic resins can change from lot-to-lot of material and due to other process variables such as post curing time. Calibration beams should be made of the same lot of material that the prototype parts are made and undergo identical post curing processes. If possible the calibration beams should be made at the same time the parts are being made by including them in the geometry file. Tests should then be performed to determine the dynamic modulus over the frequency range of interest to allow accurate scaling of the natural frequencies from the epoxy parts to the real metal parts.

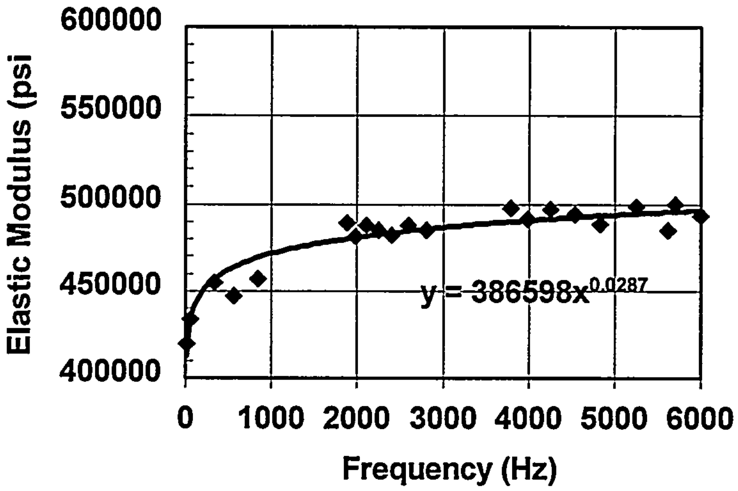

Figure 2.5 Dynamic modulus of 5180 epoxy

Mechanical Creep

Most plastics creep under static loads [3,10] which can create problems when making static stress and deflection measurements and predicting actual metal part performance. The effects of creep on measurements of a complex structure are demonstrated later in Chapter 4. A study was performed using static tensile tests on specimens fabricated with the 5180 epoxy resin to investigate the creep associated with the plastic prototype parts. Tests were performed by applying load increments and maintaining the load while measuring the change in the length with an extensiometer.

A series of one hundred pound load increments (100, 200, 300, and 400 pounds) were applied in the first experiment and the load was maintained for 20 minutes at each level. In subsequent experiments the load was increased to 200 and 300 pound increments. Data for these experiments are given in Figure 2.6. The data show the increase in strain while maintaining the load at each of the load increments. Figure 2.7 shows an expanded view of the strain for the load increment dwells of 100, 200, and 300 pounds with an analytical fit to the data superimposed with the solid line. As can be seen from the data, the creep is not excessive, but measurements of static strain and deflection data can be affected if the loads are applied for long periods of time. The average creep rate over the 20 minute load dwell was approximately 5.75 microstrain (10^{-6} in./in.) per minute for the 100 pound dwell. The average creep rates over the 20 minute load applications were approximately 18.0 and 27.5 microstrain per minute for the 200 and 300 pound loads, respectively. These results show that the creep rates increase with increasing loads (stresses) applied to the plastic parts. The 100 pound loading data shows increased scatter in the strain data due to lower signal to noise ratio of the extensiometer at the lower load levels. These results further suggest that proper scaling of the loads to insure that reasonable stresses are induced into the plastic parts, and time efficient measurements should be used when performing static testing on plastic prototype parts.

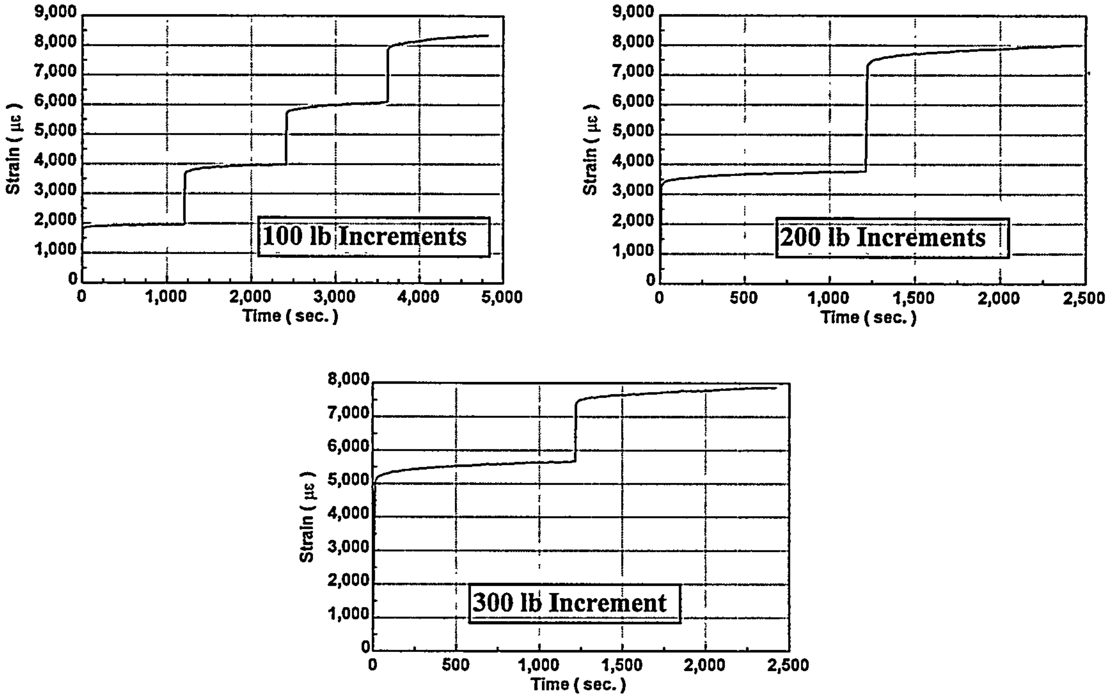

Figure 2.6. Mechanical creep with 100, 200, and 300 pound load increments

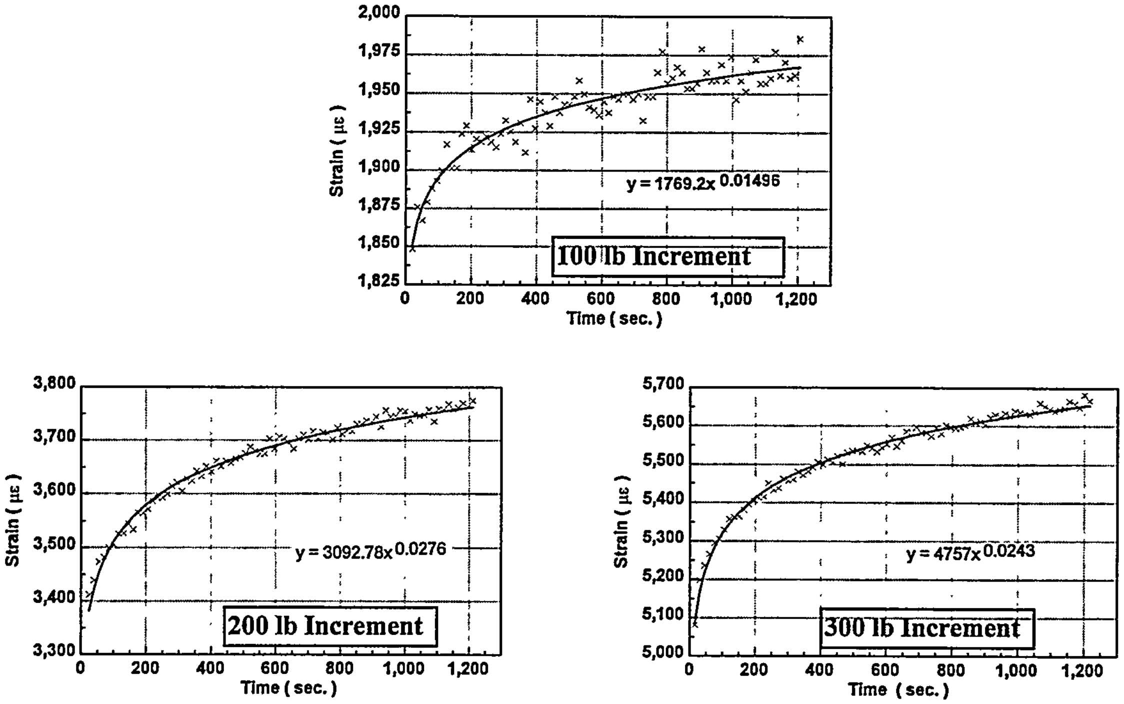

Figure 2.7. Expanded view of creep rates at 100, 200, and 300 pound tensile loads

Chapter 3

Material and Geometric Scaling Laws

Static Deflections and Stresses

The equations of equilibrium and compatibility show that the distribution of stress in the elastic state is independent of the magnitude of the loads and the scale of the model [12]. If the model (plastic part) and prototype (metal part) are geometrically similar and the distribution of the loading is the same for both, the model results can be related to the prototype following the laws of similarity.

In two-dimensional problems, the stress distribution is also independent of elastic constants if the body forces are zero or uniform. However, in three-dimensional problems the distribution of stress depends on Poisson's ratio (ν). Poisson's ratio for plastic materials such as the 5180 epoxy resin used in the stereolithography process will usually be higher (0.37 versus approximately 0.3) than most metals. The difference in values of Poisson's ratio for hard plastics such as epoxies compared to metals is usually small at room temperature and its effect can usually be neglected [12,13]. Even when Poisson's ratio for the model material is approximately 0.5, errors arising from this effect are likely to be small. If extremely accurate results are required, then the effect of the difference in Poisson's ratio needs to be examined through the use of an analytical model where Poisson's ratio can be easily changed and the sensitivity studied.

The stresses, σ_m, in the model (plastic part) are related to the stresses, σ_p, in the prototype (real part) for a two-dimensional case by:

$$\sigma_p = \sigma_m \left(\frac{F_p}{F_m}\right)\left(\frac{t_m}{t_p}\right)\left(\frac{L_m}{L_p}\right) \tag{3.1}$$

and for the three-dimensional case:
(ν = constant)

$$\sigma_p = \sigma_m \left(\frac{F_p}{F_m}\right)\left(\frac{L_m}{L_p}\right)^2 \tag{3.2}$$

where:

F = applied force, lb
σ = stress, psi
t = thickness of two-dimensional model or prototype, in
L = characteristic dimensions, in
ν = Poisson's ratio
m,p = subscripts denoting model (plastic part) and prototype (real part), respectively.

The relationship for strains is derived from the above equations using $E = \sigma/\varepsilon$ (where E is Young's modulus and, ε, is the strain giving for the two dimensional case:

$$\varepsilon_p = \varepsilon_m \left(\frac{F_p}{F_m}\right)\left(\frac{t_m}{t_p}\right)\left(\frac{L_m}{L_p}\right)\left(\frac{E_m}{E_p}\right) \tag{3.3}$$

and for the three-dimensional case the expression for the strain becomes:
(ν = constant)

$$\varepsilon_p = \varepsilon_m \left(\frac{F_p}{F_m}\right)\left(\frac{L_m}{L_p}\right)^{2}\left(\frac{E_m}{E_p}\right) \tag{3.4}$$

The deflection, δ, in the two-dimensional model is proportional to the quantity F/Et and the deflection in the prototype can be derived from the relationship:

$$\delta_p = \delta_m \left(\frac{F_p}{F_m}\right)\left(\frac{t_m}{t_p}\right)\left(\frac{E_m}{E_p}\right) \tag{3.5}$$

For a three-dimensional model , geometrically similar to its prototype, the expression for the deflection, δ, becomes:
(ν = constant)

$$\delta_p = \delta_m \left(\frac{F_p}{F_m}\right)\left(\frac{L_m}{L_p}\right)\left(\frac{E_m}{E_p}\right) \tag{3.6}$$

The relationship between the model and prototype applied forces F_m/F_p can be easily solved for from the above expressions. Plastic parts offer an advantage over metal parts in determining deflections since the required forces are much less to give equivalent deflections. This is important for correlating analytical models since the foundation (fixtures) used in the testing of plastic parts approach the ideal infinite impedance (fixed condition) relative to the stiffness of the plastic parts which is desirable for the structural analyst to assume. When tests on metal parts are used to correlate with analytical models, the stiffness of the metal parts typically approach the stiffness of the fixtures and load application machine. This often violates the fixed condition assumption and may leave the structural analyst the difficult task of modeling the fixtures and load application machine to correlate the analytical model.

Natural Frequencies and Mode Shapes

The natural frequencies of real parts can be determined accurately from plastic parts. This is one of the most valuable uses of plastic models. Only a few measurements are required to determine the frequencies of the plastic part. The acoustic velocity (velocity of sound), c , in the plastic material must be measured as a function of frequency. The acoustic velocity is equal to the square root of the ratio of the dynamic modulus of elasticity, E, to the mass density of the plastic. Except for Poisson's ratio, which has only a minor effect, the acoustic velocity is the only material property of significance [2,3,14] in natural frequency tests. The acoustic velocity is determined by measuring the frequencies of test beams made from the same lot of material as the plastic parts using techniques previously described. The scaling of natural frequencies is can be written as:

$$f_p = f_m\left(\frac{c_p}{c_m}\right)\left(\frac{L_p}{L_m}\right) \tag{3.7}$$

where the acoustic velocity, c, is:

$$c = \sqrt{\frac{Eg}{\gamma}} \tag{3.8}$$

where:

c = acoustic velocity in the material, in/sec
f = natural frequency, Hz
E = Young's modulus, psi
L = characteristic Length, in
g = acceleration due to gravity, in/sec^2
γ = specific weight, lb/in^3
m,p = subscripts denoting model (plastic part) and prototype (real part), respectively.

The estimated scaling factor, calculated from the dynamic modulus of the epoxy (see Figure 2.5), to predict steel frequencies from 5180 epoxy is shown in Figure 3.1. The scaling factor decreases from approximately 3.24 at 10 Hz to approximately 3.0 at 2000 Hz and slowly decreases at higher frequencies. A least squares analytical fit to the computed scale factors is shown with the solid line representing the equation of the fitted curve. This curve was established for one lot of material, and differences should be expected for other lots. This frequency calibration should be performed for each lot of material.

The frequency scaling factor for aluminum parts is almost the same as for steel since the acoustic velocities in steel and aluminum are almost identical (c_s / c_{al} = 1.03). The acoustic velocities in most other common structural metals such as magnesium and titanium are also very similar to steel and aluminum and a scale factor of approximately 3.0 can be used as a "rule of thumb" for most metals.

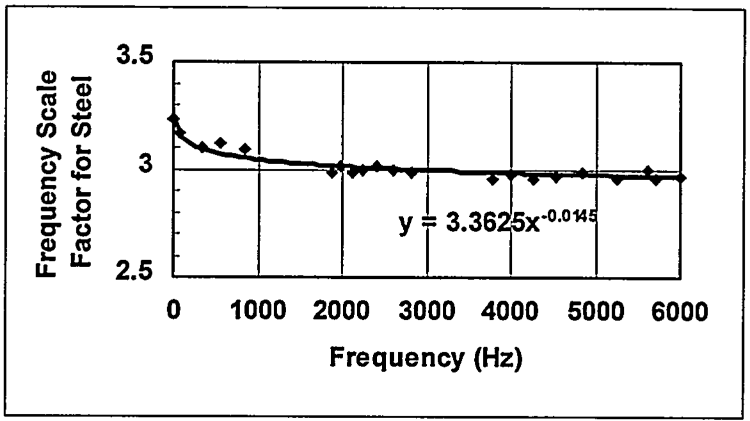

Figure 3.1. Frequency scaling factor for steel

Determination of mode shapes using transducers, typically accelerometers, require that several measurements be made at various locations on the structure during the test. The number of measurement points depends on the resolution of the mode shapes required for the application. It should be noted that the mounting of these transducers induces mass loading effects which can create errors in the measured frequencies and mode shapes which is of particular concern when testing light-weight plastic models. Examples of the effects of mass loading due to transducers are discussed later. Other non-contacting measurement techniques, discussed elsewhere this report, such as laser Doppler velocimetry eliminate the mass loading effects. Mode shapes are measures of relative displacement and are arbitrarily scaled and no further scaling is required to the actual part from the plastic part for direct correlation to be made. Ideally, the mode shapes of the plastic part and the metal part should be the same. Comparisons of measured mode shapes for the epoxy and metal parts are discussed later.

Structural Damping

Damping (internal energy loss) is the most difficult material parameter to scale from plastic to metal. In fact, damping is probably one of the least understood material properties for any material and is the most uncertain parameter measured during modal tests on metal structures. Various ways of representing energy loss are used, but the most common method is to measure damping and derive an equivalent viscous damping ratio (ζ) for use in analytical models. Experiments in this study show that for metal parts the damping is measured from .01 to 0.5 percent of critical viscous damping. The plastic parts on the other hand exhibit damping values ranging from 2.0 to 6.0 percent of critical viscous damping , thus representing differences of two orders of magnitude. The damping mechanisms at the microscopic level are not well understood and only the macroscopic (total effect) are attempted to be quantified. To understand this, one only has to think of an example of a complex part assuming the deformation of a particular vibrational mode shape which involves tension, compression, and shear deformation during vibration. Another mode shape of the same part at another frequency will involve these effects in different proportions and the resulting overall energy loss will be different even though the material and geometry of the part remains constant. The internal damping due to microscopic effects associated with the material matrix are extremely complex and not fully accounted for in modal testing theory.

The results from the experiments performed in this study do not indicate a straight forward scaling relationship for damping from epoxy to metal. Separate experiments on different structures made of steel and aluminum indicated different average damping values as compared to the epoxy results. Further studies using more controlled boundary conditions need to be performed to investigate this problem.

Chapter 4

Static Measurements

Static Tests on Flat Plate

A total of eight strain gages were mounted on both an aluminum and a 5180 Epoxy plastic part in a rectangular arrangement as shown in Figures 4.1 and 4.2. The plate was simply supported along two sides using cylindrical steel supports. Enforced deflection from 0.0 to 0.065 inches were applied at three locations on each plate and the resulting strains were measured. The loads were applied at the center of the plate, and at offsets of 0.375 inches and 1.0 inches.

Similitude requirements for strain for the same enforced displacement condition require that the measured strains (and strain distribution) be the same for the aluminum and the plastic plates. The results from the 1.0 inch offset loadings are shown in Figure 4.3. The measured strain results show fairly good correlation between the aluminum and plastic plates with the correlation improving with increasing load. Some of the error can be explained by the lack of exact positioning and orientation of the strain gages, positioning of the simple supports, and local plastic deformation of the load applicator which had a small ball bearing at the end to help eliminate friction effects due to local curvature of the test parts. The aluminum plate showed small indentations after the load applications. The plastic plate also showed slight out-of-plane warping indicating the presence of residual stresses, which can explain the improved correlation in the results at higher displacement levels. Once the residual stresses are overcome the internal stresses become more similar. However, the majority of these results are within the anticipated accuracy of approximately 20% as discussed in Reference [3] for static tests on plastic parts including all the sources of error including creep. It should be noted that the spatial stress distribution followed quite well between the plastic and aluminum plates (i.e. the relative strain amplitudes were similar for the plastic and steel measurements).

The structural stiffness of each part was determined by plotting the applied load as a function of the deflection measured near the application point and calculating the slope. The results are shown in Figure 4.4. The ratio of the measured structural stiffness of the steel to the plastic parts was 27.9 for the center load point and 28.7 for 1.0 inch offset load point. From equation (3.6) for the static load scaling the predicted stiffness ratio (proportional to the ratio of elastic moduli) is 23.1 for the elastic modulus calculated at a load rate of approximately 2 inches per minute.

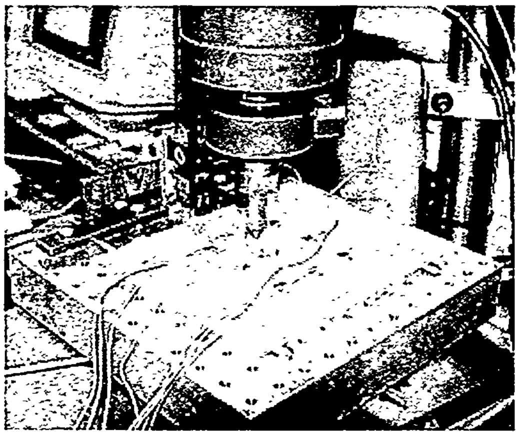

Figure 4.1 Static test setup for 5180 epoxy plate

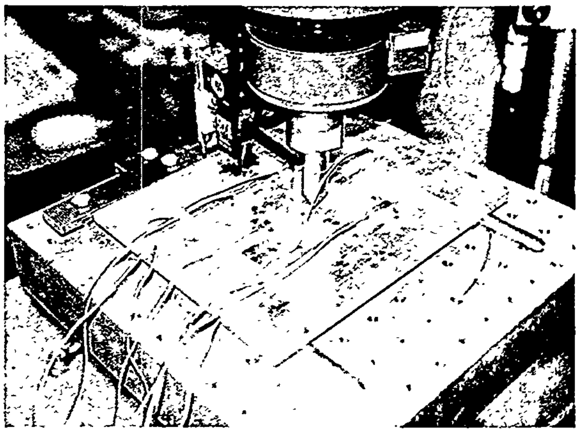

Figure 4.2 Static test setup for aluminum plate

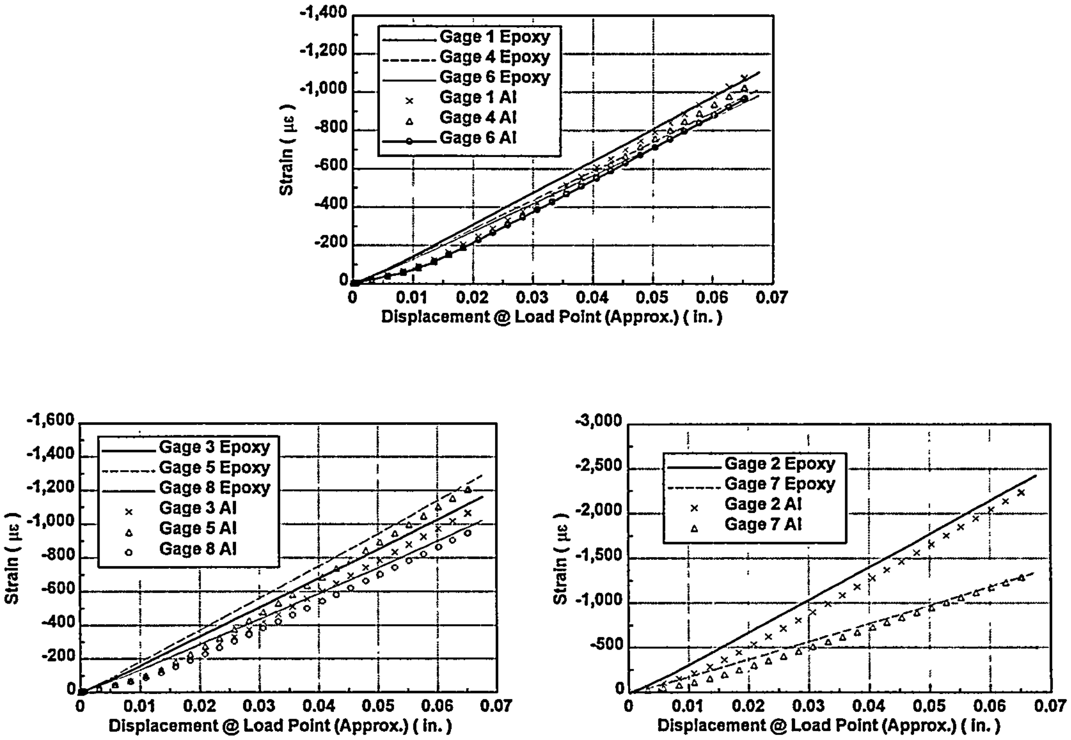

Figure 4.3 Static strain results for 1.0 inch offset loading for rectangular plate

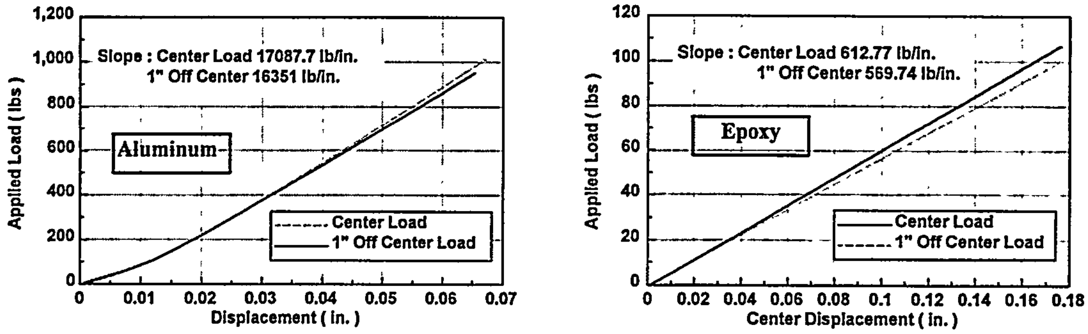

Figure 4.4 Structural stiffness of aluminum and 5180 epoxy rectangular plates

Static Tests on Fireset Cover

Similar tests as reported for the flat plates were performed on a fireset cover which houses electronic components of a development weapon system. The fireset cover represents a complex three-dimensional geometry including holes, fillets, cut-outs, etc. An array of strain gages were attached to both the stainless steel and corresponding 5180 Epoxy prototype fireset covers. The plastic part was a full scale replica of the real part with the exception of some small cutouts in a vertical rib of the fireset cover. These differences were due to the inability to obtain the exact three-dimensional model of an existing machined piece of hardware whose cost of re-machining would have been prohibitive for this study. Figures 4.5 and 4.6 show the test setups of the fireset covers installed on the load machine.

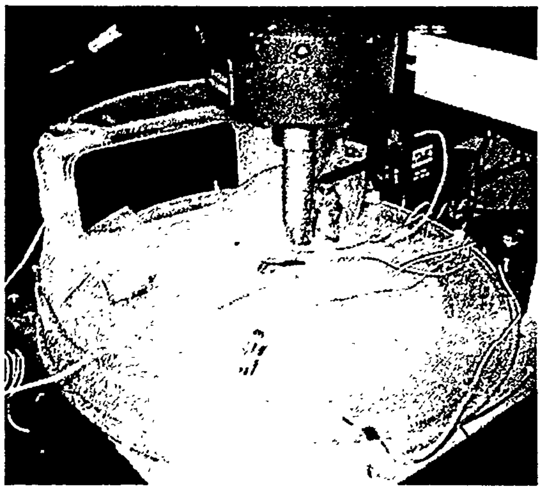

Figure 4.5. Static test setup on 5180 epoxy fireset cover

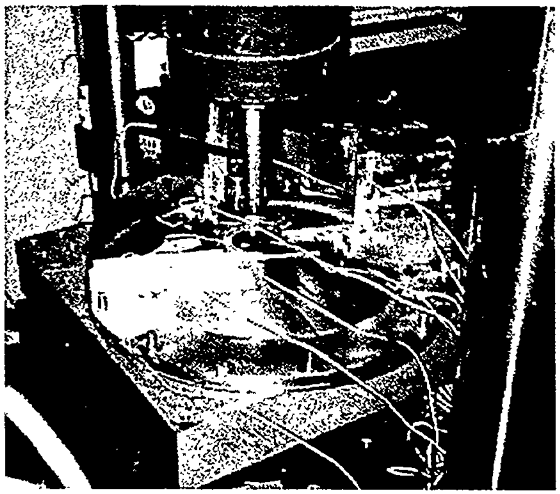

Figure 4.6 static test setup on steel fireset cover

A relative deflection measuring transducer was installed to measure the applied displacement near the load applicator with respect to the base to minimize the effects of deflection of other parts of the test machine. Strain gages were bonded at seven locations at selected points on each part. The load was applied at two locations on the parts; the first was near the center of the parts (Load Point A) and the second was offset approximately 0.50 inches (Load Point B) from the center loading. The load was increased in increments of .010 inches with dwells at each increment until the maximum displacement of .040 inches was reached. The maximum level of .040 inches was chosen to limit the stresses below yield in the metal part. After load application it was noticed that there was a plastic indentation in the steel part indicating local yielding. The results for the strain gages for load point A are shown in Figure 4.7. The results showed fairly good agreement for all the strain gages, with most in the range of 20%.

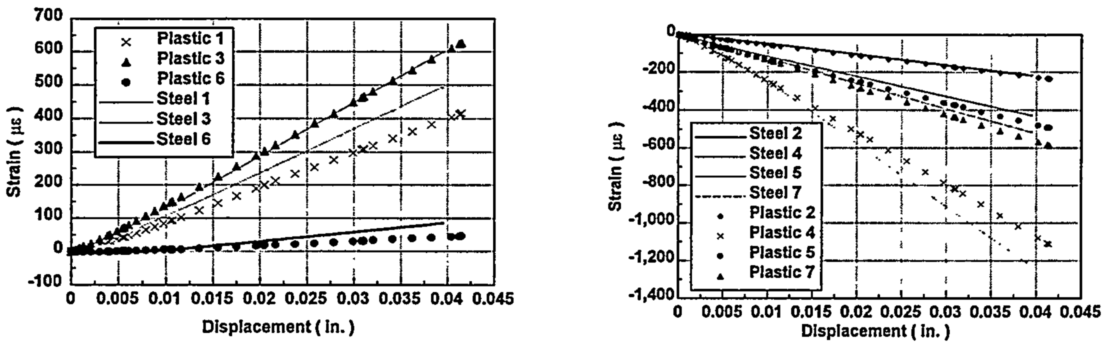

Figure 4.7. Static strain results for load point A for steel and epoxy fireset covers

The structural stiffness of each part was determined by plotting the applied load as a function of the deflection measured near the application point and calculating the slope. The results are shown in Figures 4.8 and 4.9. The ratio of the measured structural stiffness of the steel to the plastic parts was 63.4 for load point A and 62.1 for load point B. From Equation 3.6 for the static load scaling the predicted ratio is 69.0 for a load rate of approximately 2 inches per minute. The small steps in the plots for the plastic parts are an indication of mechanical creep occurring at the intermediate load dwells.

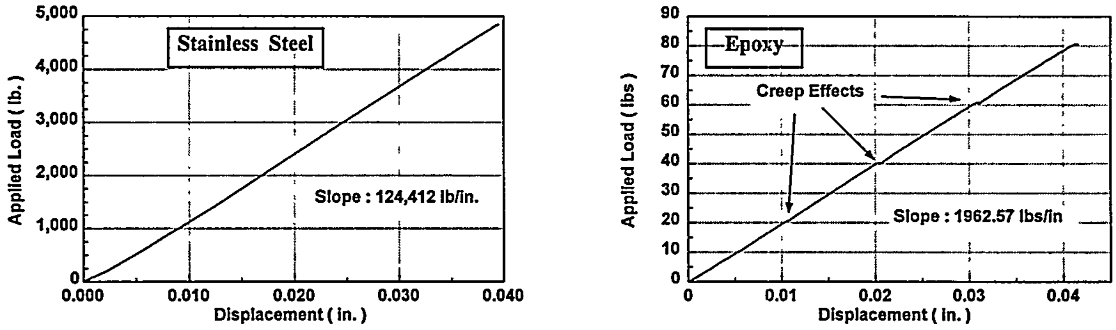

Figure 4.8. Structural stiffness for load point A for steel and epoxy fireset covers

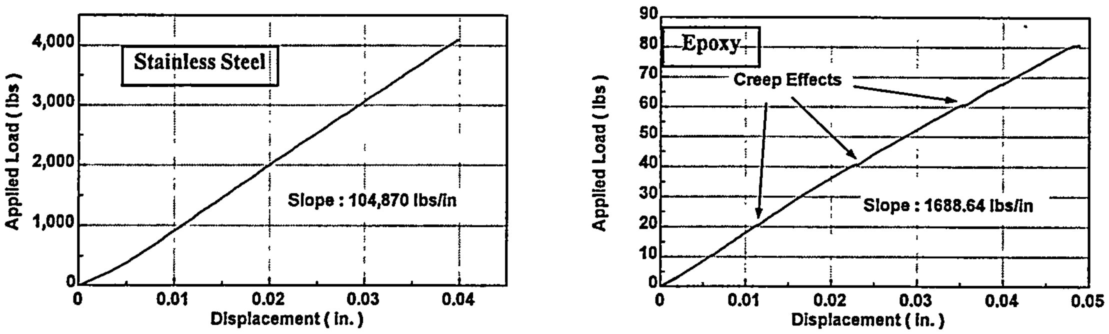

Figure 4.9. Structural stiffness for load point B for steel and epoxy fireset covers

Bicycle Crank ESPI Studies

The bicycle crank originally came to Sandia's attention via a Small Business Assistance Request. With its holes, fillets, and complicated relief structure, it seemed to be an ideal structure for this study. The FE model was developed in-house and several rapid prototype stereolithography parts had already been made to study the stereolithography process. This previous study also included the "Quick Cast" process, in which the geometry file is used to make a part from an epoxy designed for casting. A mold is made from that part and the epoxy is fired out, similar to the lost-wax process. The mold is then used to cast the metal part. Cranks of aluminum and steel had been made, and several more were made specifically for this project. Comparisons of static response of the metal and epoxy parts will be discussed here, and dynamic comparisons will be discussed in the next chapter.

Static deformation shapes. For the static ESPI studies, the cranks were fixtured in an aluminum frame, bolted down by all 5 spider holes as shown in Figure 4.10. The illumination and observation directions were both nearly normal to the plane of the object, so the fringes represent deformation contours of about 0.26 microns per fringe. An attempt was made to apply a load similar to the pedal load the crank would see in use. A bolt was inserted through the pedal hole, and weights added to a basket at the end of the bolt (3.375 inches from the crank surface). The crank loads were adjusted to produce the same amount of twist at the axle hole (approximately 3 fringes, or 0.77 microns, across the crank) for the steel and epoxy parts, in an attempt to verify the deformation scaling predicted by Equation (3.6). Figure 4.11 shows a type 5180 crank pedal loaded at 20gm, Figure 4.12 shows a steel crank at 600gm, and Figure 4.13 an aluminum crank loaded at 250gm. The deformation patterns in the spider area are similar, but the loadings do not agree with the ratios that would be predicted by the relative material stiffnesses. It appears that the relative stiffness of the fixture played a significant role in the amount of twist in the spider area, making the softer epoxy part appear stiffer than it should. This assumption is borne out by the fact that the epoxy part shows significantly higher fringe density further out the crank (to the left), indicating that the deformations are actually not identical throughout the part. The Epoxy crank was loaded approximately twice as much, and the aluminum part was loaded approximately 1.25 times as Equation (3.6) would predict.

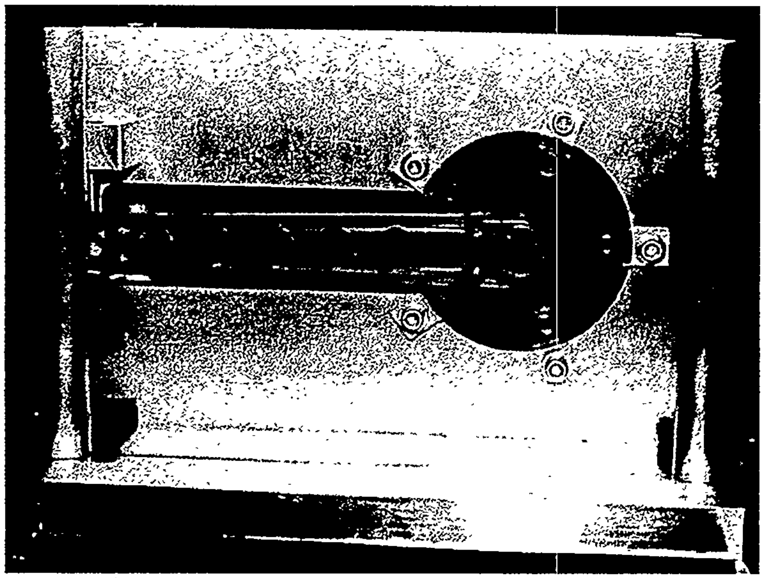

Figure 4.10. Epoxy bicycle crank in fixture

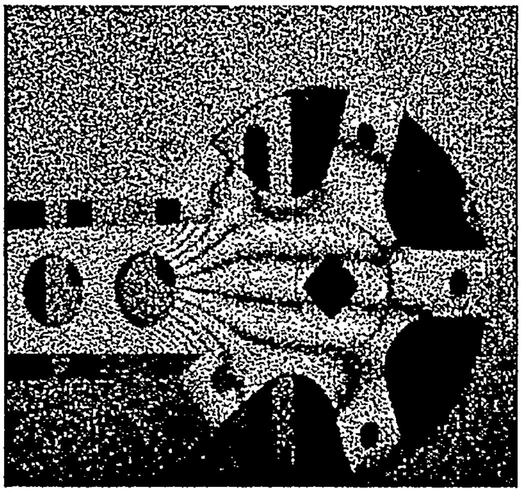

Figure 4.11. Epoxy bike crank with 20 gm pedal load

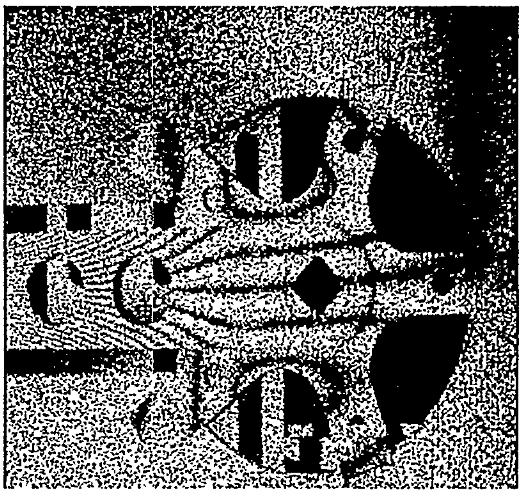

Figure 4.12. Steel bike crank with 600 gm pedal load

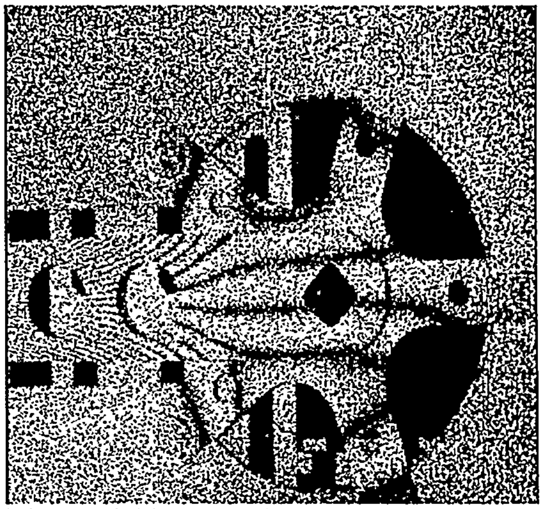

Figure 4.13. Aluminum bike crank with 250 gm pedal load

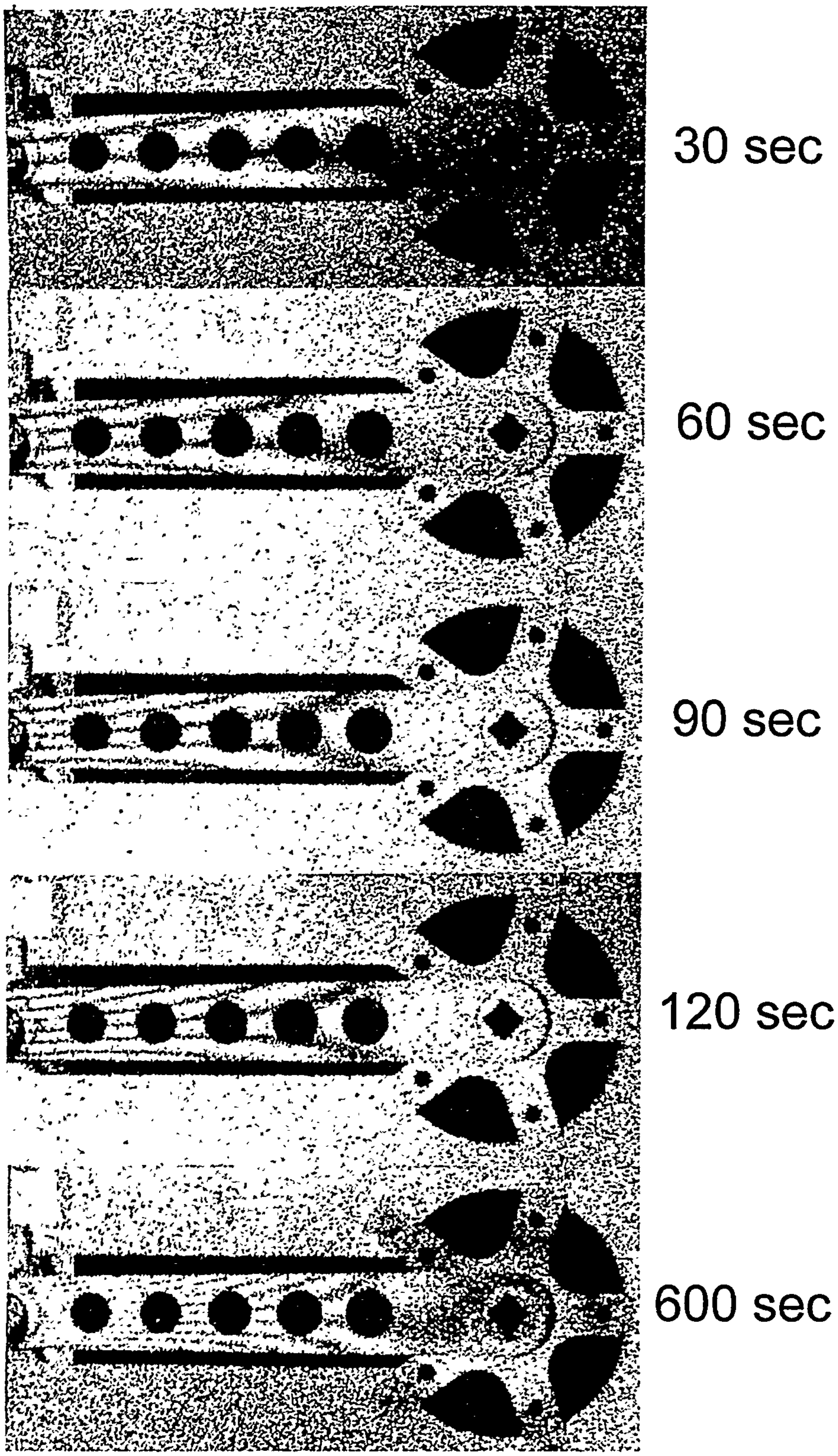

Figure 4.14. Epoxy bike crank, creep deformation at various times after removal of 36 gm pedal load

This study demonstrated the undesirable creep properties of the epoxy materials. To study creep, a 36gm pedal load was applied to the type 5170 crank. Immediately after the load was applied, the reference frame was stored. Figure 4.14 shows the deformation due to creep after 30, 60, 90, 120, and 600 seconds. For the first two minutes, the creep was essentially linear. At ten minutes, the deformation was approximately 3.5 times what it was at one minute.

To study deformation shapes only, without the influence of modulus scaling, the same out of plane deformation was applied to the aluminum, steel, and epoxy cranks, with a screw moving the pedal end outward. The results are shown in Figures 4.15, 4.16, and 4.17 for type 5180 epoxy, aluminum and steel respectively. The fringe patterns are essentially identical, indicating that the rapid prototype parts predict deformation shapes accurately. A finite element model was also run with the same displacement, with results shown in Figure 4.18.. This analytical deformation shape was input to the COBRA simulation code for ESPI. Figure 4.19 is the predicted fringe pattern. The similarity between this figure and the actual data indicates that the FE model was also able to predict the static deformation well in this case.

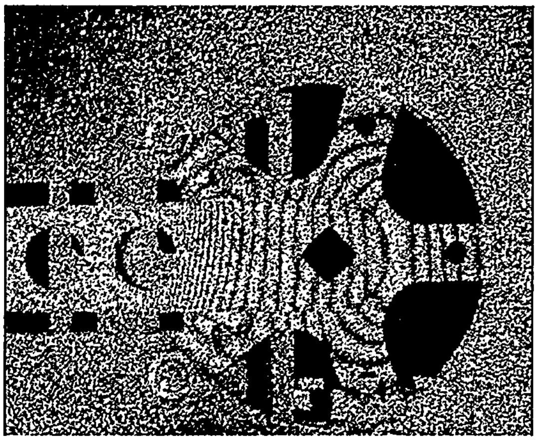

Figure 4.15. Epoxy bike crank, out of plane deformation.

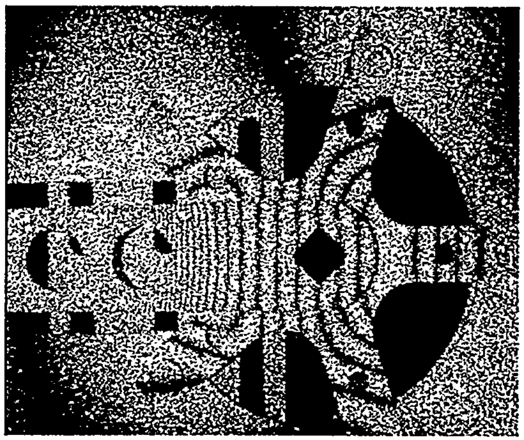

Figure 4.16. Aluminum bike crank, out of plane deformation.

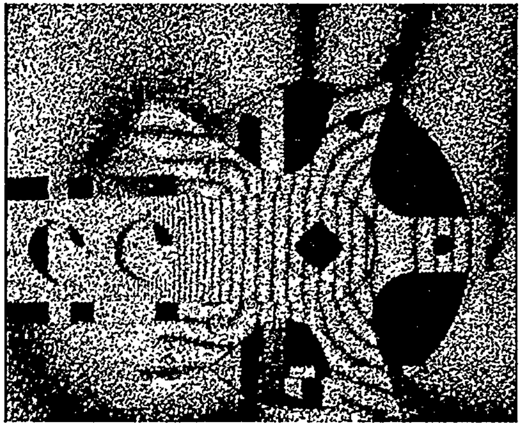

Figure 4.17. Steel bike crank, out of plane deformation.

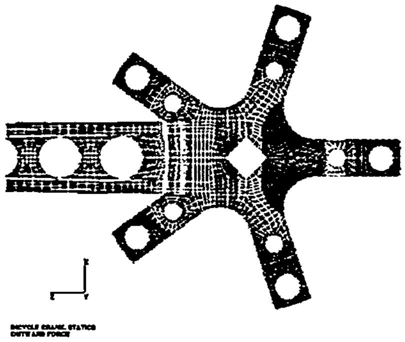

Figure 4.18. Finite element model of bike crank with out of plane deformation. Contours represent displacement, (crank bar is saturated).

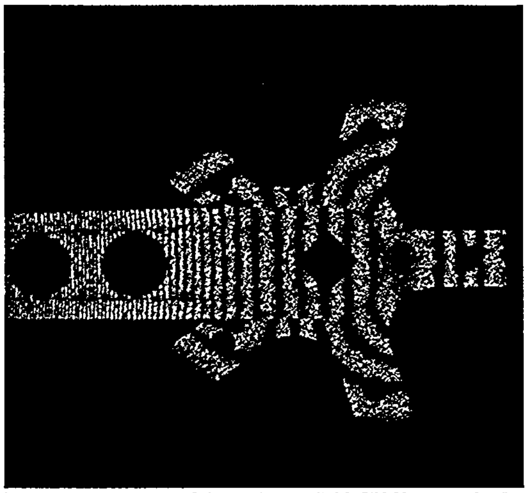

Figure 4.19. Simulated ESPI result by COBRA, based on model in Figure 4.18

Thermoelastic Imaging

Ometron demonstrated their SPATE system at Sandia, using the bike crank as an example object. The equipment was used to visualize the stress pattern in epoxy and steel cranks undergoing out of plane strain at a frequency well below any resonances. The cranks were fixtured as shown in Figure 4.20, with an electromagnetic shaker providing an oscillatory force at the pedal end. The area of interest was the crank bar near the axle and the spider, as shown. Figures 4.21 and 4.22 are stress pattern images of the epoxy and steel cranks, and indicate that the epoxy part accurately represents the stresses in the steel part.

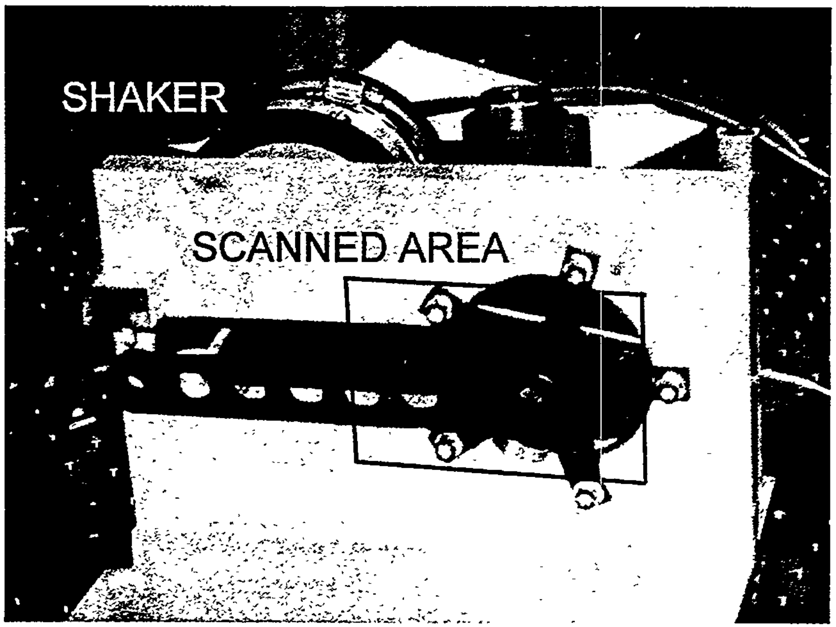

Figure 4.20. Setup for thermoelastic imaging of bike crank.

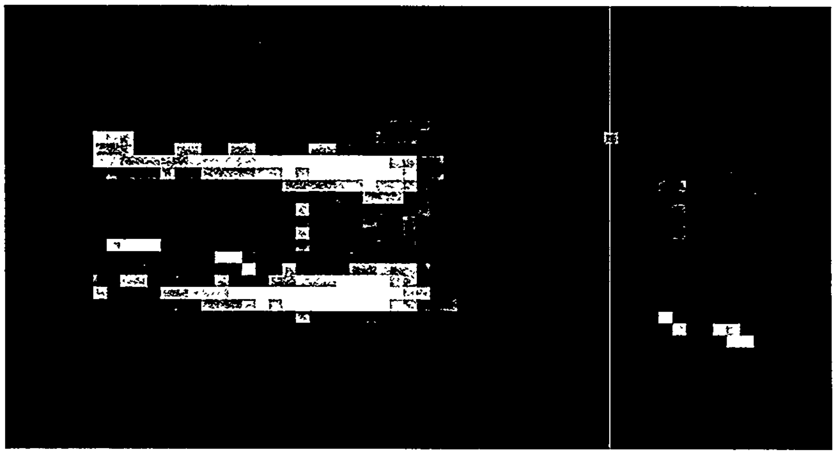

Figure 4.21. Thermoelastic stress pattern image of rapid prototype epoxy bike crank.

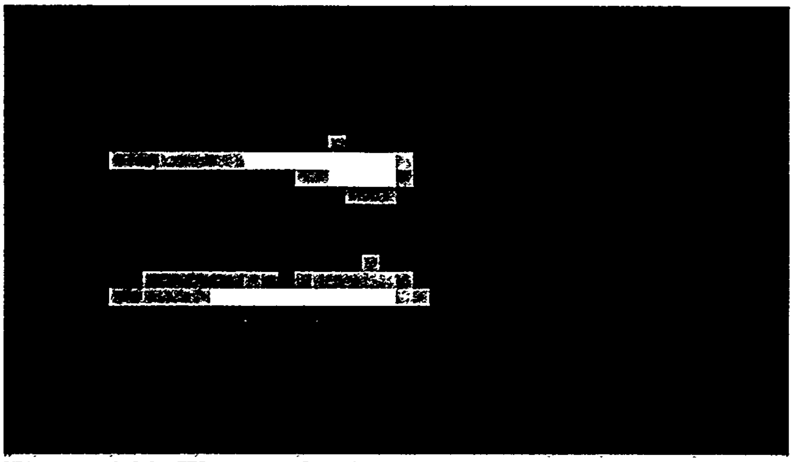

Figure 4.22 Thermoelastic stress pattern image of steel bike crank cast from stereolithography master.

Chapter 5

Dynamic Measurements

Rectangular Plate

Modal tests to determine frequency scaling laws were performed on free-free rectangular plates made of aluminum and 5180 epoxy. The size of the plates (9.0" length x 7.19" width x 0.25" thickness) was selected to give widely spaced natural frequencies to allow accurate determination of the frequencies and damping. A total of nine accelerometers were placed in a rectangular pattern on the plates as shown in Figure 5.1. The plates were supported on soft foam to simulate free-free boundary conditions. A small instrumented hammer was used to impact the plates at selected locations. The resulting impact force and accelerometer response measurements were analyzed with a digital signal analyzer to measure the modal (natural) frequencies and damping.

The results are summarized in Table 5.1. The modal frequencies and damping for the first five modes are shown for the aluminum and epoxy plates. The ratio of frequencies is essentially constant (3.00 to 3.21) over the frequency range of 500 to 1500 Hz. The damping values for the epoxy and the aluminum parts are higher than for other experiments performed in the study partly due to the fact that the entire surface of the plates was supported by the foam which added additional damping to the results.

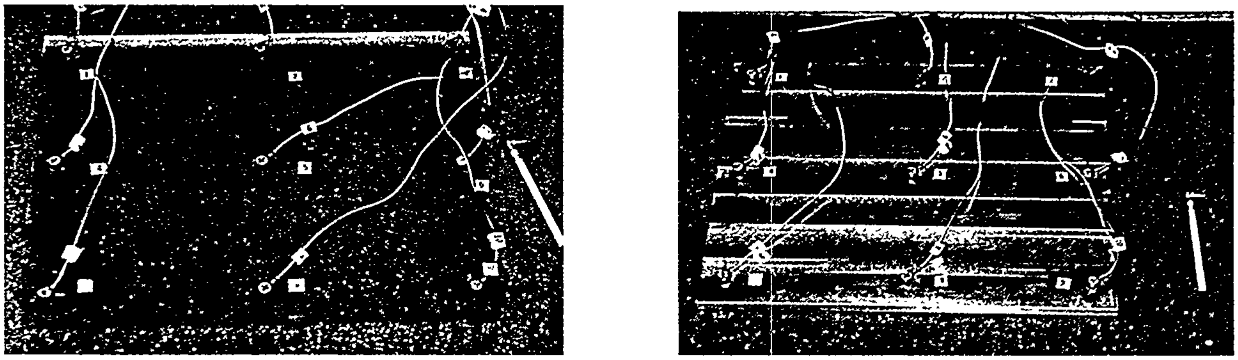

Epoxy **Aluminum**

Figure 5.1. Modal test setup photograph of aluminum and epoxy plates

Mode Number	Alum. Freq. (Hz)	Epoxy Freq. (Hz)	Freq. Ratio (f_{al}/f_{epoxy})	Alum. Damping (%)	Epoxy Damping (%)	Damping Ratio (ζ_{al}/ζ_e)
1	535.5	178.5	3.00	1.44	4.67	0.31
2	687.0	220.6	3.11	0.81	3.77	0.21
3	1139.7	377.4	3.02	0.55	3.43	0.16
4	1278.7	398.5	3.21	0.50	4.82	0.10
5	1502.5	470.1	3.20	0.57	2.89	0.20
Avg.			**3.11**	**0.77**	**3.92**	**0.20**

Table 5.1. Frequency and damping results for 5170 epoxy and aluminum plates

Bicycle Crank Modal Studies

The aluminum, steel, and type 5180 epoxy bicycle cranks, previously described for the static experiments, were used to evaluate frequency scaling and mode shape similarities. Accelerometers were placed on each part as shown in Figure 5.2 and the parts were impacted with an instrumented hammer. The parts were supported on soft foam to simulate free-free boundary conditions. Modal frequencies and damping were computed using a structural dynamics signal analyzer. The measured frequencies and damping ratios are shown in Tables 5.2 and 5.3. The measured driving point Frequency Response Functions (FRFs) for the plastic and steel parts near the end of the bicycle crank where the pedal attaches are shown in Figure 5.3. Comparisons of the scaled FRFs using scaling laws for the elastic modulus and a nominal damping ratio are shown in Figure 5.4. The scaling was performed by adjusting the modal parameter table by the average scaling ratios of the epoxy crank for frequencies (3.14) and damping (0 .04) and then synthesizing the new analytical "scaled" FRF. The results show that the frequencies scale closely, but the scaling of the amplitudes are not as consistent (note the logrithmic scale) due to the uncertainties and errors in the damping estimates as previously discussed.

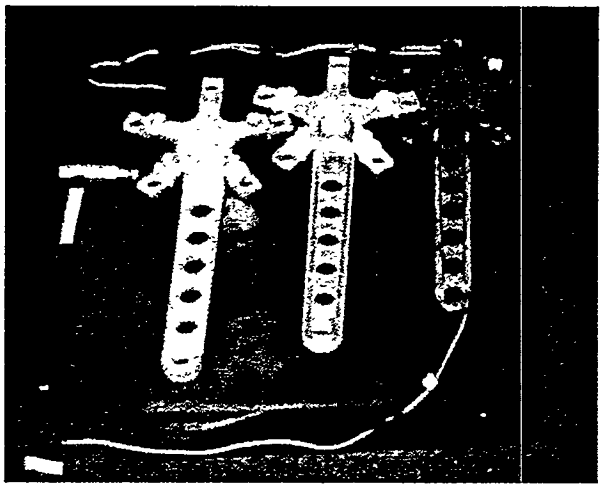

Figure 5.2. Modal test setups for aluminum, steel, and 5180 epoxy bicycle cranks

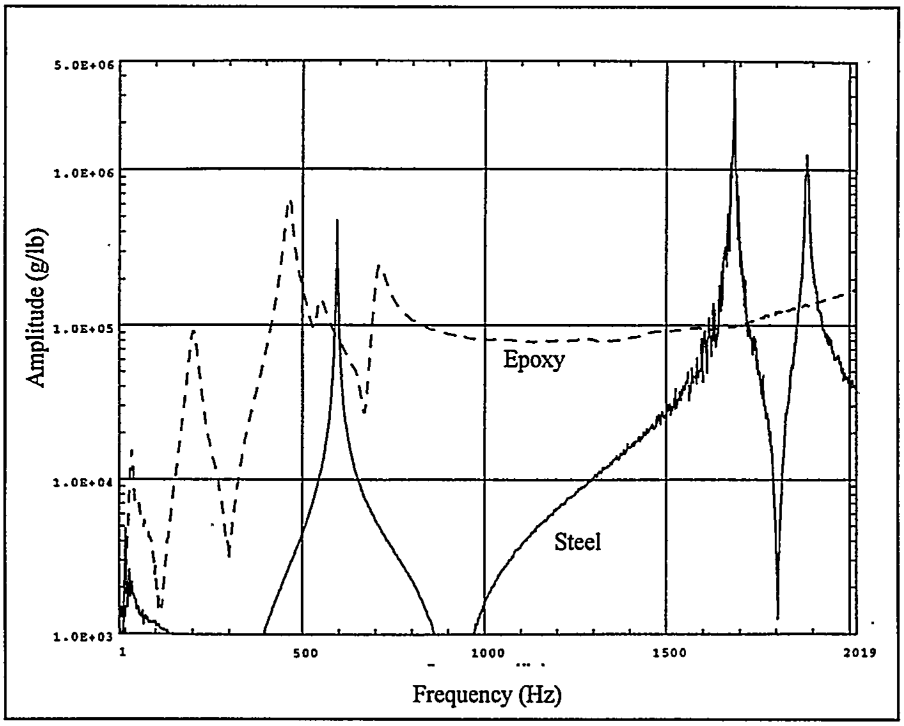

Figure 5.3. Unscaled frequency response functions of steel and epoxy bicycle cranks

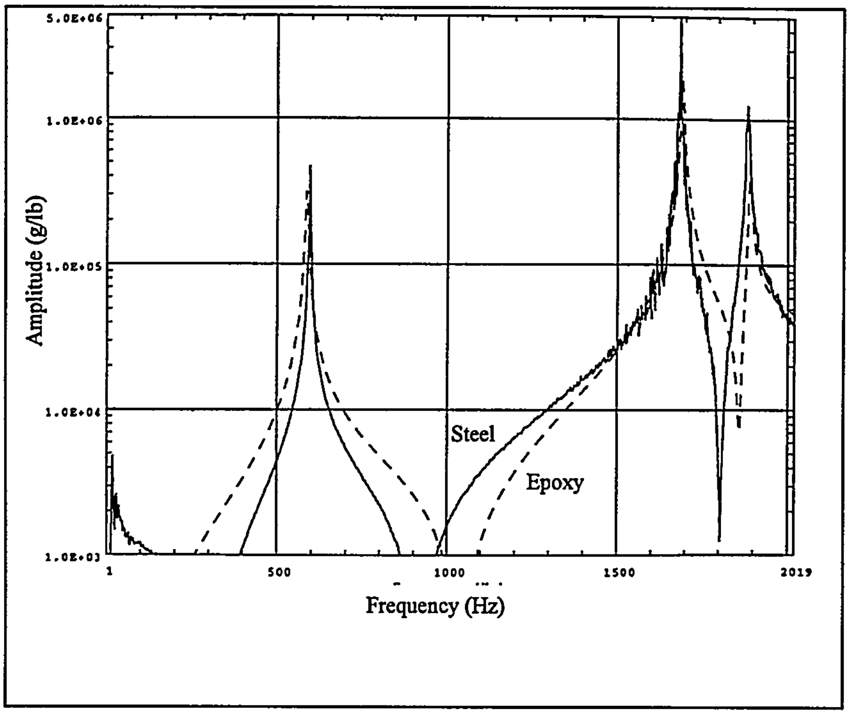

Figure 5.4. Scaled frequency response functions of steel and epoxy bicycle cranks

Mode No.	Alum. Freq. (Hz)	Steel Freq. (Hz)	Epoxy Freq. (Hz)	Freq. Ratio Alum./Steel (f_{al}/f_s)	Freq. Ratio Alum./Epoxy (f_{al}/f_e)	Freq. Ratio Steel/Epoxy (f_s/f_e)
1	648.8	633.6	201.9	1.024	3.21	3.14
2	1599.0	1589.3	470.0	1.001	3.40	3.38
3	1660.9	1674.1	552.0	0.992	3.01	3.03
4	1847.9	1814.8	593.1	1.018	3.12	3.06
5	2022.8	1991.4	650.0	1.016	3.11	3.06
6	2304.2	2249.1	712.0	1.024	3.24	3.16
Avg.				**1.013**	**3.18**	**3.14**

Table 5.2. Frequency results for aluminum, steel, and 5170 epoxy bicycle cranks

Mode No.	**Alum. Damp. (%)**	**Steel Damp. (%)**	**Epoxy Damp. (%)**	**Damping Ratio Alum./Steel** (ζ_a/ζ_s)	**Damping Ratio Alum./Epoxy** (ζ_a/ζ_e)	**Damping Ratio Steel/Epoxy** (ζ_s/ζ_e)
1	0.408	0.392	5.70	1.04	0.072	0.069
2	0.133	0.152	2.10	1.14	0.063	0.072
3	0.123	0.059	2.10	2.08	0.059	0.028
4	0.096	0.073	2.40	0.76	0.040	0.030
5	0.152	0.078	3.97	1.95	0.038	0.020
6	0.062	0.049	2.10	1.27	0.030	0.023
Avg.	**0.162**	**0.134**	**3.07**	**1.37**	**0.050**	**0.040**

Table 5.3. Damping results for aluminum, steel, and 5170 epoxy, bicycle cranks

Bicycle Crank ESPI Operating Shape Visualization

ESPI was used to visualize the first few vibratory operating shapes of the rapid prototype bike cranks. The aluminum crank was hung from one of the spider holes on a stinger attached to the Wilcoxon shaker. This configuration simulated the free-free condition. Figure 5.5 shows the first bending mode at 658 Hz, and Figure 5.6 shows the first twisting mode at 1647 Hz. (Note that the bright areas are the node lines, and the fringes are essentially vibration amplitude contours with about 0.26 micron peak-to-peak contour intervals.) These shapes correspond well to the first two modes predicted by the FE model, shown in Figure 5.7 and 5.8. The frequencies also agree with the modal results from impact testing (649 Hz and 1599 Hz), especially when the expected lowering of frequency by transducer mass loading is considered.

Figure 5.5. ESPI visualization of first bending mode of aluminum bike crank at 658 Hz.

Figure 5.6. ESPI visualization of first twisting mode of aluminum bike crank, at 1647 Hz.

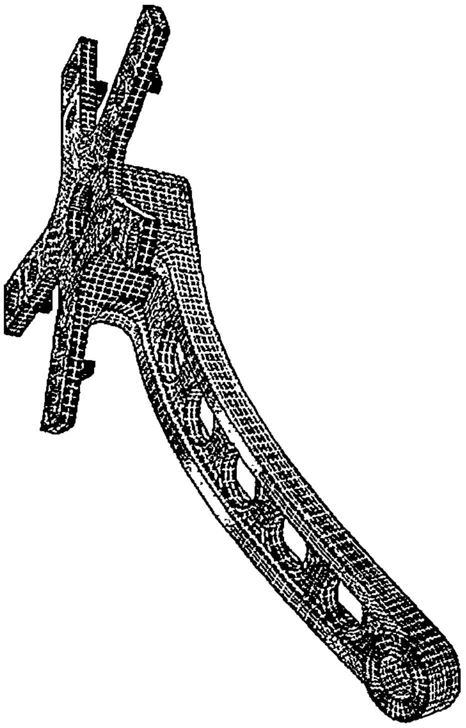

Figure 5.7. FE model of crank, first bending. Intensities represent strain.

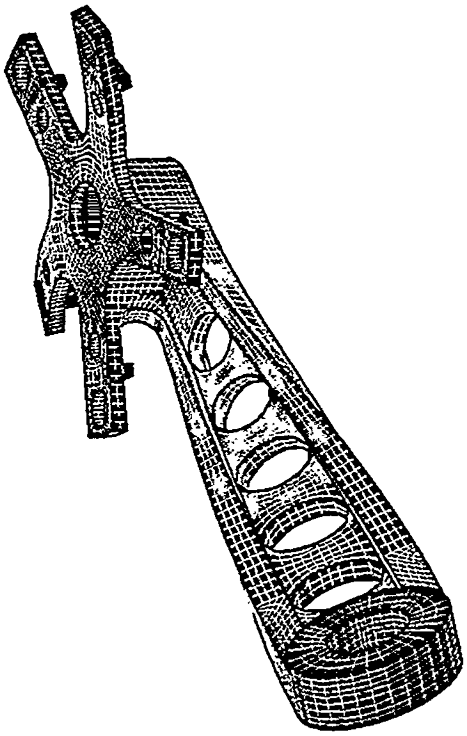

Figure 5.8. FE model of crank, first twisting. Intensities represent strain.

Fireset Cover Modal Studies

A series of modal studies was performed on the fireset covers that were previously discussed in the static testing case study. A total of 52 small accelerometers were mounted in the same locations on each of the stainless steel and 5180 epoxy parts, as shown in Figures 5.9 and 5.10. The parts were supported on soft foam to simulate free-free boundary conditions. The parts were impacted with a small instrumented hammer and the resulting input force and response accelerations were measured with a structural dynamics signal analyzer. Frequency response function (FRF) measurements were analyzed and the free-free modal parameters for the first five modes were computed including frequencies, damping ratios, and mode shapes.

A comparison of frequency and damping is shown in Table 5.4. A comparison of the first two mode shapes is shown in Figures 5.11. The results show that the ratio of the frequencies is essentially constant over the test bandwidth, but higher than the anticipated frequency ratios shown in Figure 3.1 The frequencies were then measured with only three accelerometers placed on the part. These frequencies are listed in Table 5.5, showing much closer agreement with the predicted frequency ratios. These results are further evidence of the effect of mass loading where mounted transducers can create errors, in particular for the light weight plastic parts where the transducer mass becomes significant with respect to the mass of the plastic parts. The damping values for the metal are much less than the plastic which was expected, but showed more consistent results than for some of the other experiments. It is speculated that due to the configuration the reduced interaction with the foam support aided the improved correlation. The mode shapes show very good agreement between the epoxy and steel prototypes. These results correlate well with the results using the ESPI system discussed below.

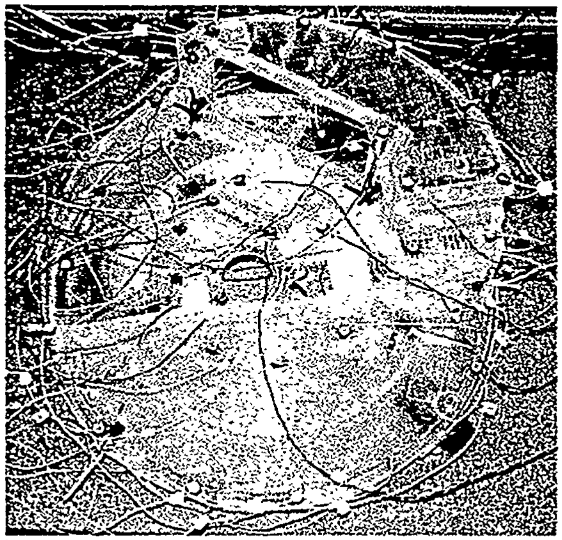

Figure 5.9. Modal test setup on 5180 epoxy fireset cover

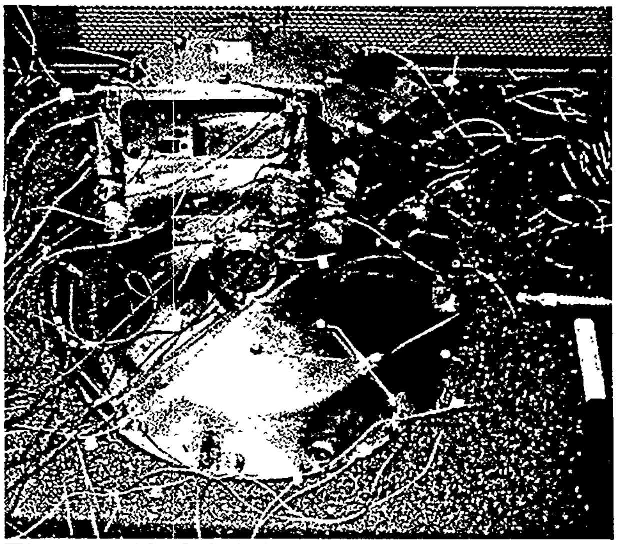

Figure 5.10. Modal test setup on steel fireset

Mode No.	Steel Frequency (Hz)	Epoxy Frequency (Hz)	Frequency Ratio (f_s/ f_e)	Steel Damping (%)	Epoxy Damping (%)	Damping Ratio (ζ_e/ζ_s)
1	428	128	3.34	0.47	2.88	0.16
2	485	147	3.30	0.46	2.85	0.16
3	816	244	3.38	0.28	2.38	0.12
4	877	270	3.25	0.30	2.74	0.11
5	1034	320	3.23	0.23	2.54	0.09
Avg.			**3.30**	**0.30**	**2.68**	**0.13**

Table 5.4. Frequency and damping comparisons for fireset covers

Mode No.	Steel Frequency (Hz)	Mass-loaded Epoxy Frequency (Hz)	Unloaded Epoxy Frequency (Hz)	Mass Loaded Frequency Ratio (f_s/f_e)	Unloaded Frequency Ratio (f_s/f_e)
1	428	128	136	3.34	3.14
2	485	147	159	3.30	3.04
3	816	244	261	3.38	3.12
4	877	270	289	3.25	3.03
5	1034	320	343	3.23	3.01
Avg.				**3.30**	**3.07**

Table 5.5. Mass loading effects on frequencies of fireset covers

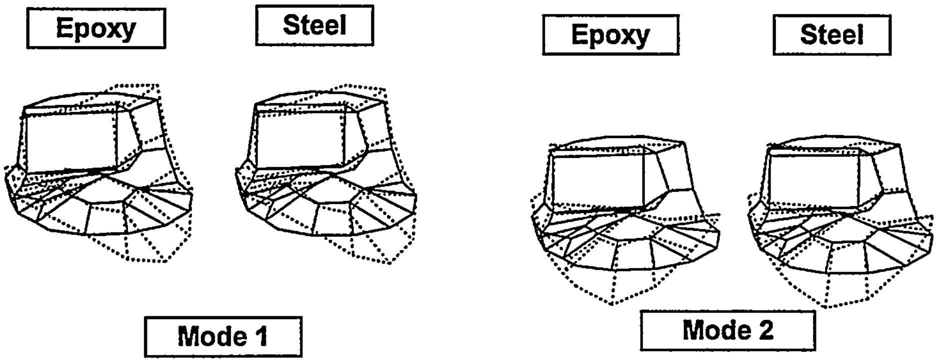

Figure 5.11. Mode shapes of epoxy and steel fireset covers

Fireset Cover ESPI Operating Shape Visualization

The vibratory operating shapes of the metal and epoxy fireset covers were also visualized and compared using ESPI. The parts were fixtured vertically and excited acoustically using a speaker placed behind the part as shown in Figure 5.12. This provided a totally non-contact excitation and measurement method. The ESPI system was arranged so the sensitivity vector was normal to the base plane of the cover, so this experiment is only sensitive to the out of plane component of the vibration.

Figure 5.13 shows operating shapes corresponding to six of the lower modes of the structure, again with the bright areas of the images representing node lines. In general, the shapes are similar. The higher damping of the epoxy was a greater problem for this complex shape than for the bike crank or turbine wheel (discussed later in this section), since the modes tended to be relatively close in frequency. The operating shapes for the epoxy part flowed smoothly from one mode to the next as excitation frequency was increased, making it difficult to identify separate modes. The epoxy operating shapes in the figure were chosen as the best match to the metal operating shapes, which were well separated in frequency, hence well defined. Table 5.6 compares the modal analysis results from Table 5.5 with the ESPI frequencies. The frequencies agree reasonably well, considering the difficulty of identifying the resonances in the epoxy part.

	Modal Analysis Results		**ESPI Results**	
Mode No.	**Steel Frequency (Hz)**	**Unloaded Epoxy Frequency (Hz)**	**Steel Frequency (Hz)**	**Epoxy Frequency (Hz)**
1	428	136	431	149
2	485	159	490	160
3	816	261	824	271
4	877	270	not identified	not identified
5	1034	343	1045	321

Table 5.6. Comparison of frequencies from conventional modal analysis and ESPI operating shape visualization.

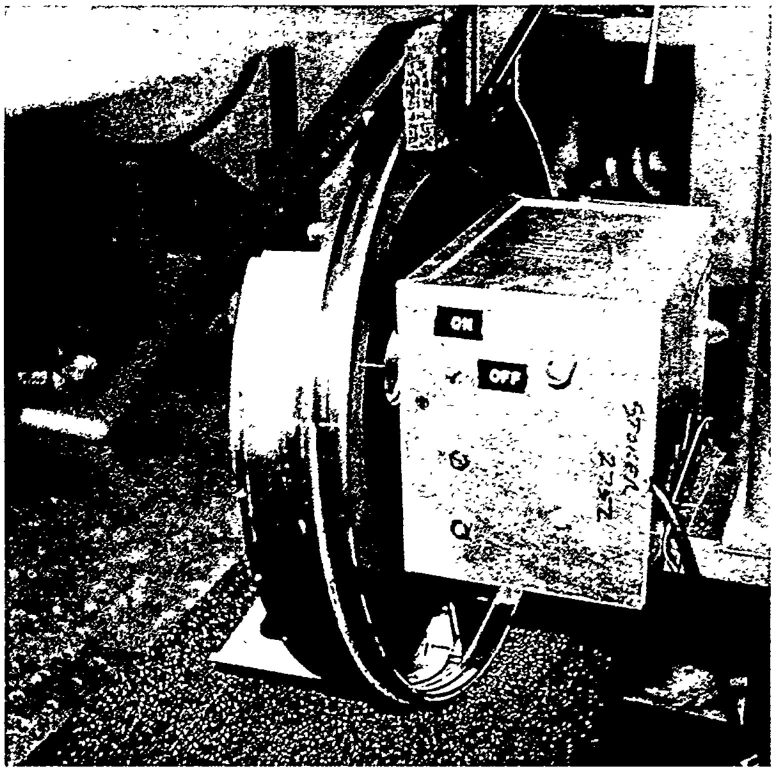

Figure 5.12. Excitation for ESPI operating shape visualization of fireset cover provided by non-contact acoustic energy.

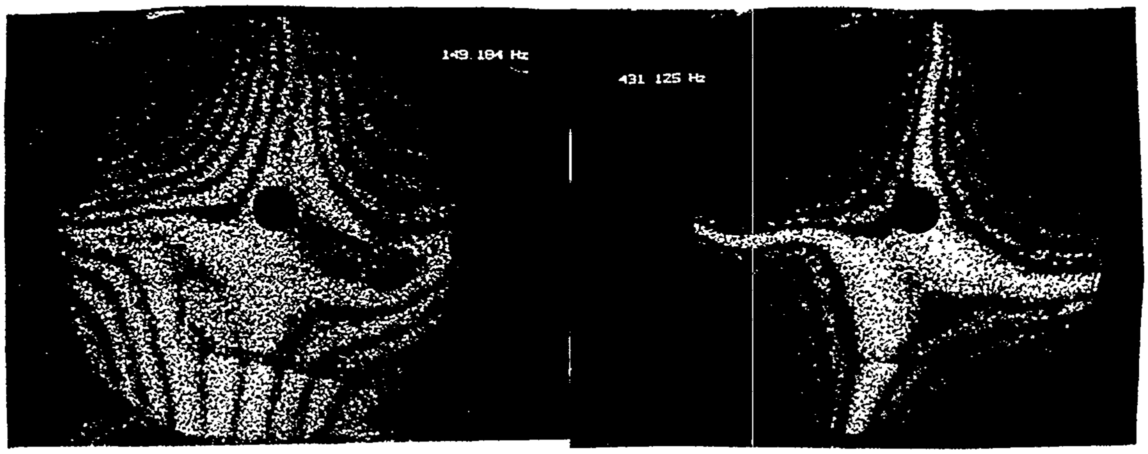

Plastic, 149 Hz　Metal, 431 Hz

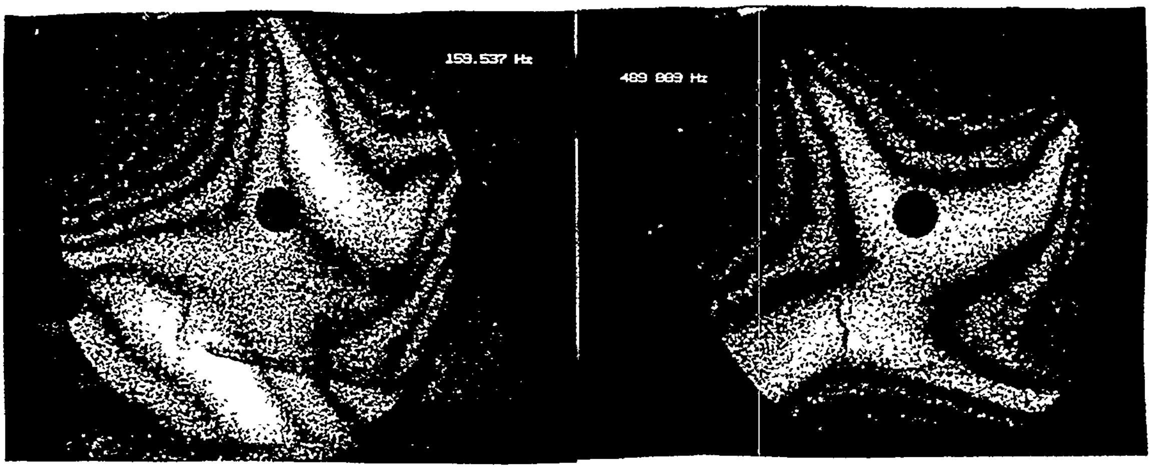

Plastic, 160 Hz　Metal, 490 Hz

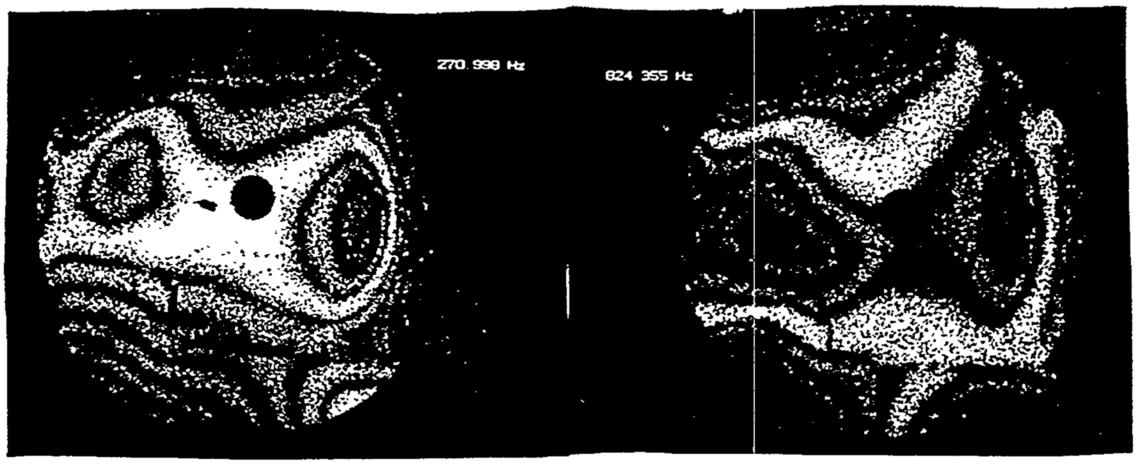

Plastic, 271 Hz　Metal, 824 Hz

Figure 5.13. Vibration operating shapes of steel and epoxy fireset covers

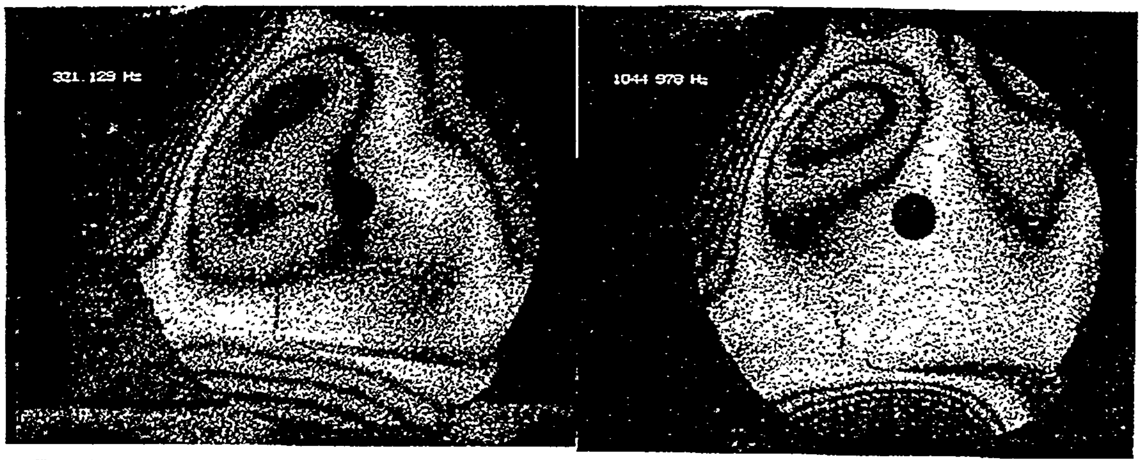

Plastic, 321 Hz

Metal, 1045 Hz

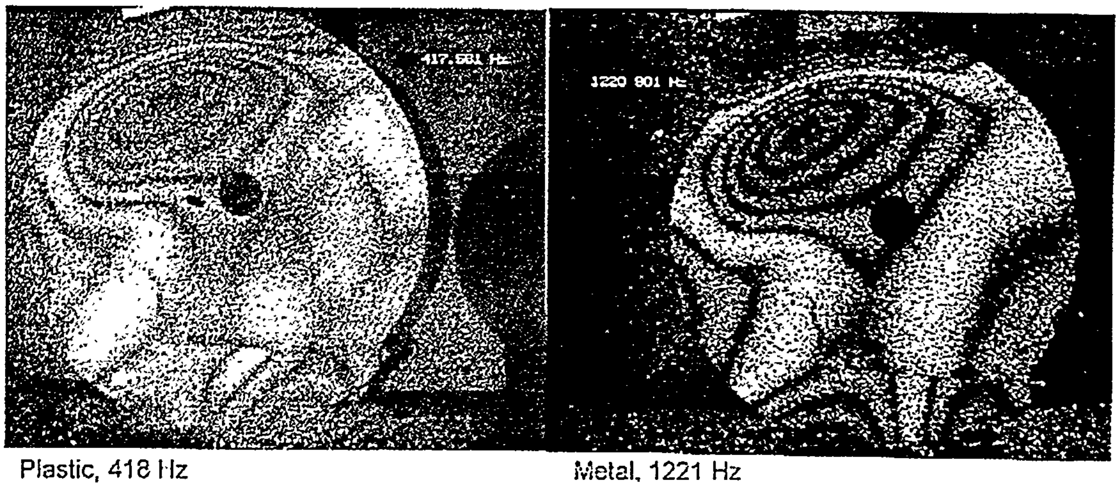

Plastic, 418 Hz

Metal, 1221 Hz

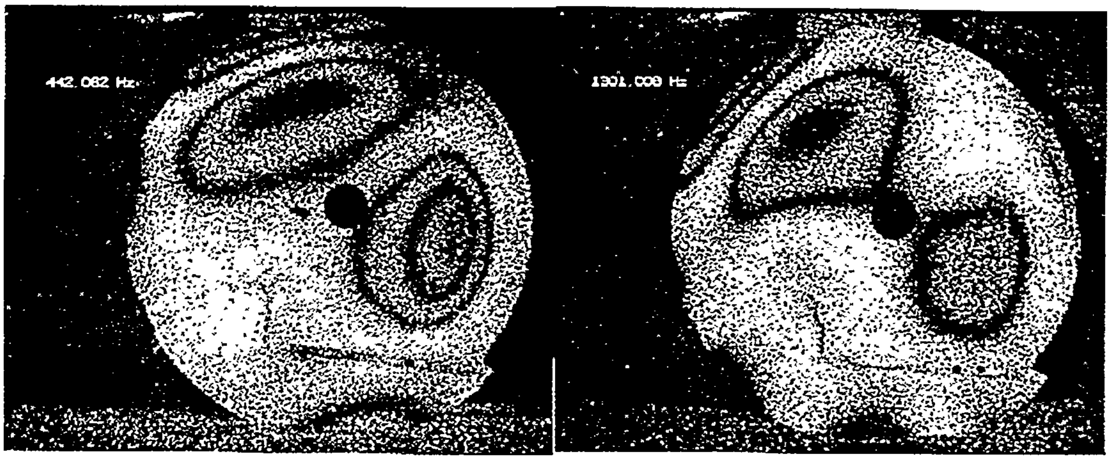

Plastic, 442 Hz

Metal, 1301 Hz

Figure 5.13 continued

Turbine Wheel Non-Contact Measurements

The turbine wheel originally came to Sandia through the National Machine Tool Partnership (NMTP). The original part is machined from titanium, and is about 15 cm in diameter. It is the final output turbine of an industrial air compressor, and is designed to run as high as 70,000 rpm. The problem that the manufacturer sought help with was a premature failure of the disk, apparently caused by high frequency fatigue. There was no obvious drive mechanism for the cracking in the disk periphery. Using both holometry and ESPI, an analysis of vibratory operating shapes was done. Due to the low damping of the titanium structure, the operating shapes were essentially equivalent to mode shapes. This analysis showed that the first bending mode of the blades was at essentially the same frequency as one of the higher plate modes--this mode is shown in Figure 5.14. A subsequent re-design of the turbine with a slightly thicker base plate effectively separated these modes as shown in Figure 5.15. (While the short duration of the NMTP projects did not allow time to prove that this was the cause of the failures, it was a plausible drive mechanism for the fatigue cracking-- in normal operation the blades do see fluid impulses at the frequency required to drive the first bending mode.) Note that a noncontacting measurement was the only feasible way to perform this measurement. A mechanical accelerometer would have mass loaded the turbine blade sufficiently to make the frequency measurement invalid.

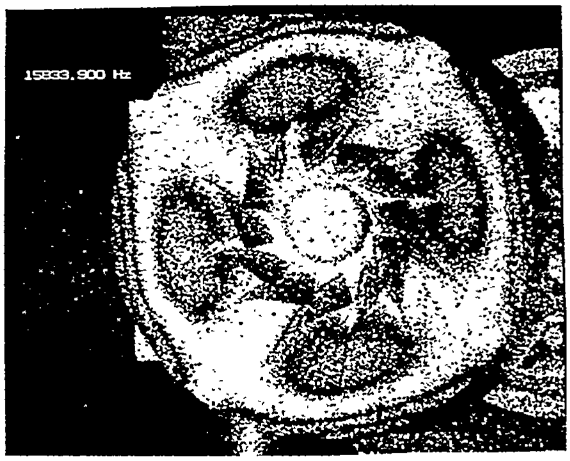

Figure 5.14: Vibration shape at blade resonance--original turbine wheel design

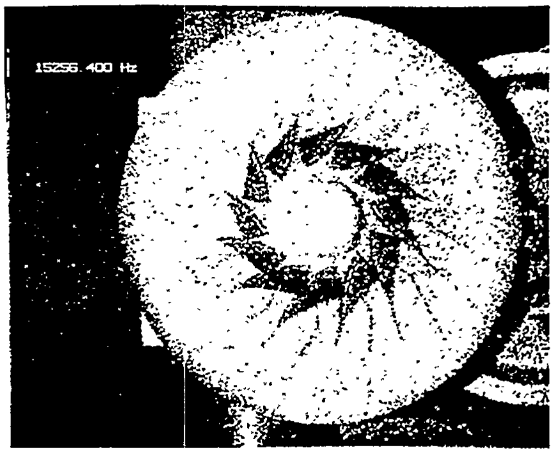

Figure 5.15: Vibration shape at blade resonance--modified turbine wheel design

The turbine wheel seemed to be an ideal real-world part to study the rapid prototype test process, including frequency scaling, geometric part scaling, and transducer mass-loading. A geometric model (of the original design) was obtained from the manufacturer, and several duplicate parts and a two times (2X) geometric scaled part were made via stereolithography, using Ciba-Geigy 5180 resin. The metal and epoxy parts are shown in Figure 5.16.

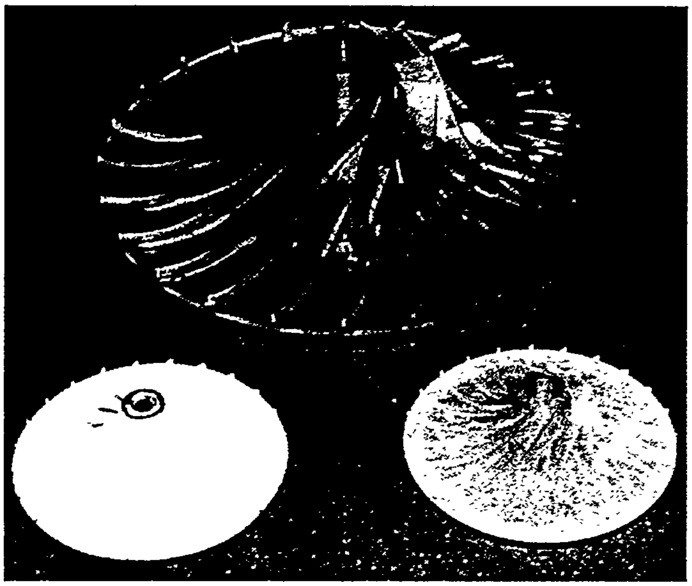

Figure 5.16. Metal, epoxy, and 2X epoxy turbine wheels.

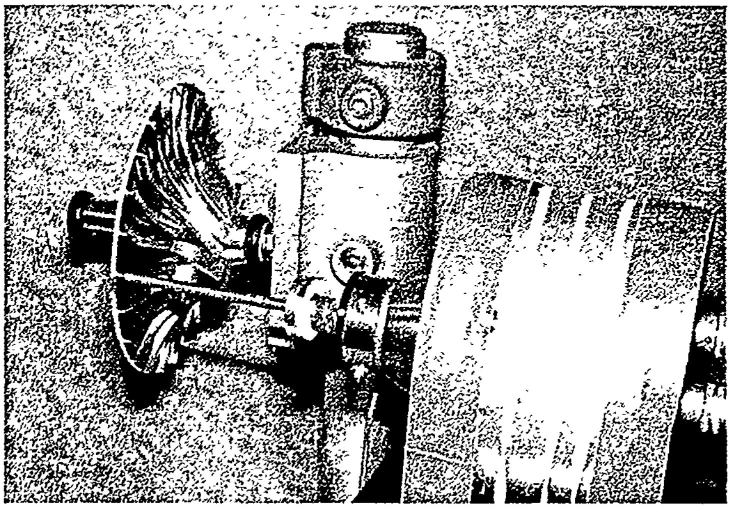

Figure 5.17. Excitation method for vibration shape study of turbine wheels.

ESPI Operating Shape Visualization of Epoxy Turbine Wheel. The goal of this experiment was to determine whether the rapid prototype model would exhibit the same operating shape behavior as the metal part, and whether the frequency and geometric scaling predictions would hold. Of particular interest was whether a rapid prototype part might have helped to predict the blade-disk coupling exhibited by the metal part. The 1X epoxy turbine wheel was fixtured in the same way as the metal wheel, as shown in Figure 5.17. This consisted of supporting the wheel on a 1/4-20 shaft with rubber grommets isolating the wheel from the shaft. Vibratory excitation was provided by a Wilcoxon model F4/F7 electromagnetic/piezoelectric shaker through a stinger held in contact with the turbine wheel by mechanical preload. For this test, the excitation was sinusoidal, varied by hand while observing the video monitor. Since the ESPI image is real time, an entire sweep takes only a few minutes, pausing at the resonances to store the image. It can be highly beneficial to the analyst or designer to see these full field operating shapes in real time, without having to wait on post-processing of conventional modal data.

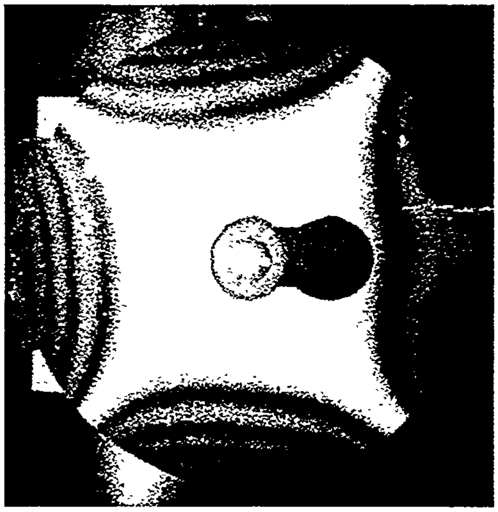

Figure 5.18a. Metal turbine wheel, 6.0 kHz

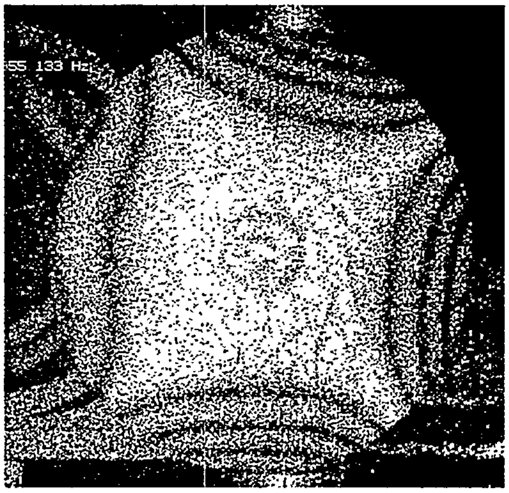

Figure 5.18b. Epoxy turbine wheel, 1.95 kHz

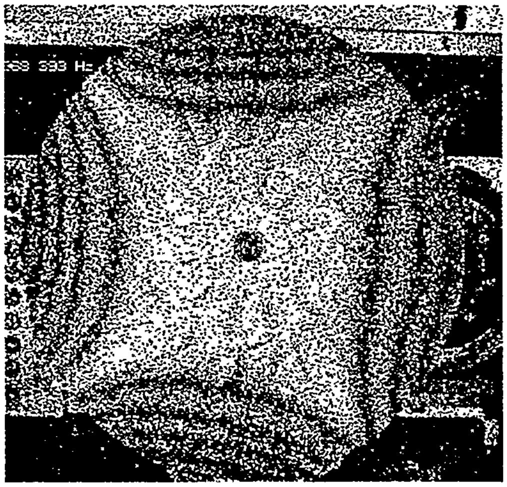

Figure 5.18c. Epoxy turbine wheel, 2X size, 0.97 kHz

The general plate operating shapes of the epoxy parts are quite similar to those of the metal parts. Figure 5.18 shows the 0/4 (lowest) plate mode for the metal, 1X epoxy, and 2X epoxy part. The slight asymmetry is caused by the stinger--note that it is the same for all 3 parts (considering the fact that the stinger is on the left in the 1X epoxy part, and on the right in the other 2 figures). Resonant frequencies for the various modes are compared in Table 5.7.

Mode shape	**Metal freq. (kHz)**	**Epoxy freq. (kHz)**	**freq. ratio (f_{Metal}/f_{Epoxy})**	**2X Epoxy freq. (kHz)**	**2X/1X Epoxy freq. ratio (f_{2X}/f_{1X})**
0/4	5.98	1.92	3.11	0.98	1.96
0/6	6.73	2.22	3.03	1.10	2.02
0/8	7.66	2.65	2.89	1.29	2.05
0/10	8.76	3.11	2.81	1.48	2.10
0/12	10.3	3.80	2.71	1.78	2.13
0/14	12.2	4.50	2.71	2.08	2.16
0/16	14.3	5.21	2.74	2.42	2.15
1st blade	15.3	5.33	2.87	2.59	2.06
1/4	15.8	5.59	2.83	2.69	2.08
0/18	NA	6.16		2.82	2.18
0/20	19.2	7.13	2.69	NA	
2nd blade	22.8	8.23	2.77	NA	

Table 5.7. Resonant frequencies for metal and epoxy turbine wheels. Mode shape refers to "radial antinodes"/"circumferential antinodes".

The frequency scaled very well between the metal and both the 1X and 2X epoxy models, as per Equation (3.7). The frequency ratios tended to decrease with frequency as predicted in Chapter 3. The predicted geometric scaling ratio of 2.0 between the 1X and 2X wheels was closely matched. Even the details of the higher blade bending modes are well represented by the epoxy parts, as can be seen by comparing the 3rd blade mode in the metal part, Figure 5.19a with the same mode in the plastic part, Figure 5.19b. Figure 5.19c shows the 5th blade mode in the metal part, demonstrating the resolution available with the ESPI technique.

In these swept-sine tests, the high Q (low damping) of the metal part causes the modes to appear and disappear with very little frequency change, with essentially no part motion (fringes) at frequencies between modes. Hence, the operating shapes very closely represent the mode shapes. In the epoxy parts, however, the broad resonances overlap, and the operating shapes flow continuously from one to the next as the frequency is varied, with no clear separation. The blade modes overlap several plate modes in the epoxy parts. Becoming visible at 5140 Hz and extending through 5670 Hz, they couple with the 0/16 plate mode at 5206 Hz, as well as with the 1/4 mode at 5600 Hz. Figure 5.20 shows the 1-4 mode in the epoxy part, with both the 0-16 plate mode and blade modes also participating. From this, it must be concluded that, while the blade modes might have been observed and hence been studied more closely, the epoxy part performance would probably not have directly predicted the blade-plate coupling that occurred in the high-Q metal part. (Use of the LDV system, with a modal analysis of the broad band data, might have allowed this prediction to be made.)

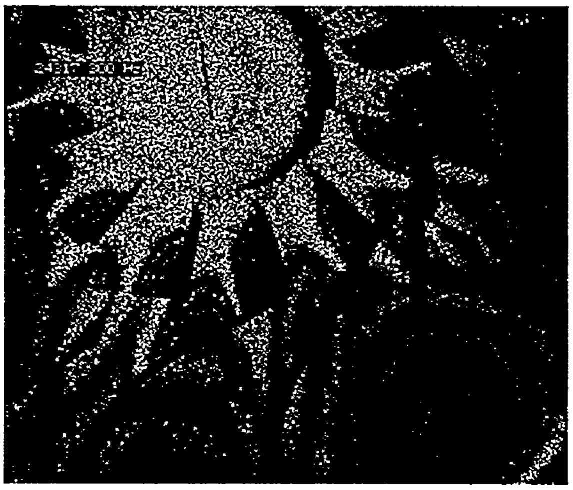

Figure 5.19a. 3rd blade bending mode, metal turbine wheel

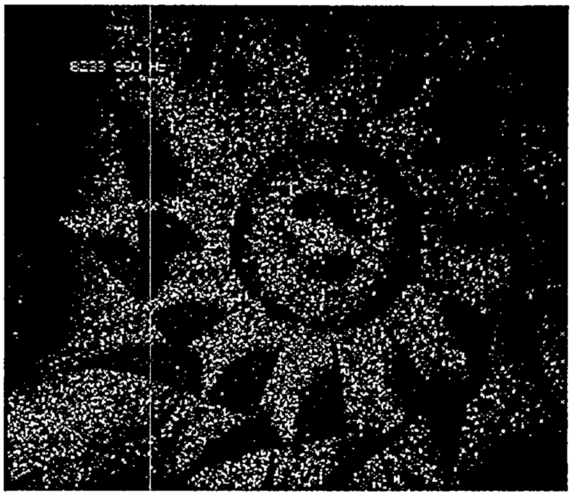

Figure 5.19b. 3rd blade bending mode in epoxy turbine wheel

Figure 5.19c. 5th blade bending mode in metal turbine wheel

Transducer Mass Loading Effects. Both ESPI and LDV were used to study the effects of mass-loading by transducers on the metal and epoxy turbine wheels. To obtain detailed modal information on the turbine wheel, as part of the NMTP project, three Endevco model 2250 transducers were attached to the back (non-blade) side of the metal turbine wheel. Including the aluminum strain-isolation blocks used to mount them, each transducer's mass was 1.8 gm, which seemed insignificant relative to the 520 gm mass of the turbine. ESPI visualization shows that even one transducer has an effect, however. Figure 5.21a shows the lowest ("0/4") plate mode of the metal turbine with no transducers, at 5890 Hz. Note the symmetry relative to the shaker position at the 3 o'clock position. The addition of only one transducer (at approximately the 10 o'clock position) splits this lower mode into two spatially orthogonal modes at 5562 and 5830 Hz, as shown in Figure 5.21b and 5.21c. Addition of two more transducers lowers the frequency of both orthogonal components to 5409 and 5547 Hz, an error of about 8%! Similar conclusions about mass loading are drawn in the section describing the modal test of the fireset cover.

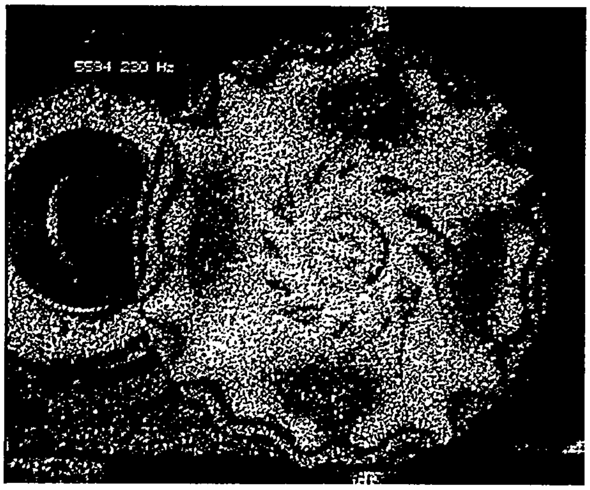

Figure 5.20. Multiple modes in plastic wheel at 5594 Hz

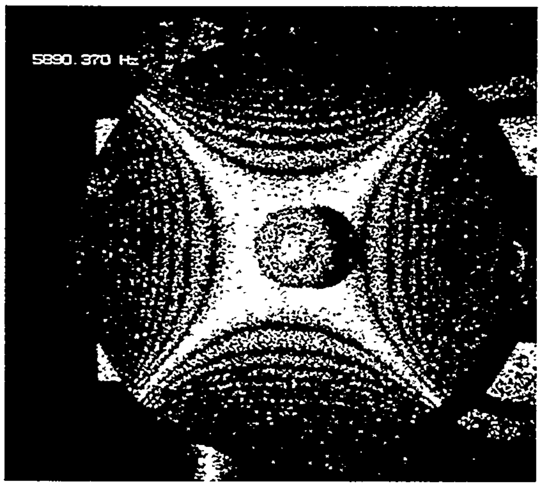

Figure 5.21a Metal turbine wheel, no transducers, 5890 Hz

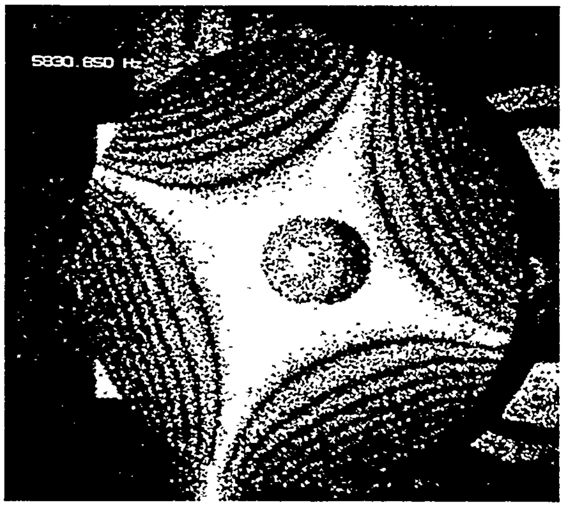

Figure 5.21b. Metal turbine wheel, one transducer, 5830 Hz

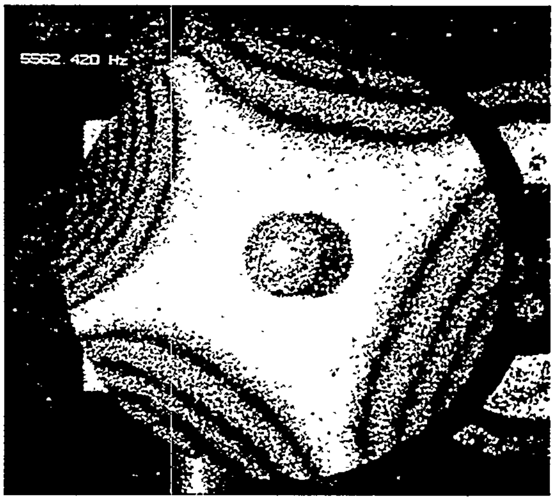

Figure 5.21c. Metal turbine wheel, one transducer, 5562 Hz

The LDV was also used on the turbine wheels, to verify that this instrument could be used to get valid data on rapid prototype parts, and to further study the effects of transducer mass loading. The turbine wheel was mounted and driven the same way as for the ESPI studies, and the LDV arranged with its sensitivity vector approximately normal to the plate. Excitation was continuous random with a Hanning window, with 10 averages for this experiment.

To compare the LDV results with conventional transducer data, LDV data was taken on a transducer mounted to the epoxy turbine, with the LDV illuminating the transducer. Since the LDV reads velocity, the LDV data had to be differentiated once (by multiplication in the frequency domain by $j\omega$) to compare with the transducer data. Figure 5.22 shows a comparison between transducer and laser frequency response function (FRF) data, with the force measured at the Wilcoxon shaker in both cases. This experiment sometimes resulted in the two curves overlying within a linewidth, and other times there was some difference, but in all cases the curve shapes were essentially the same. LDV data was also taken on the epoxy turbine directly opposite a transducer location (on the back side of the plate), with the transducer in place and again with it removed, to study mass loading effects. A representative FRF is shown in Figure 5.23. Note the significant difference in response amplitude at higher frequency, and the frequency shift at several of the resonances, caused by the mass of the transducer. These FRFs also show the broad, highly damped modal characteristic of the epoxy parts.

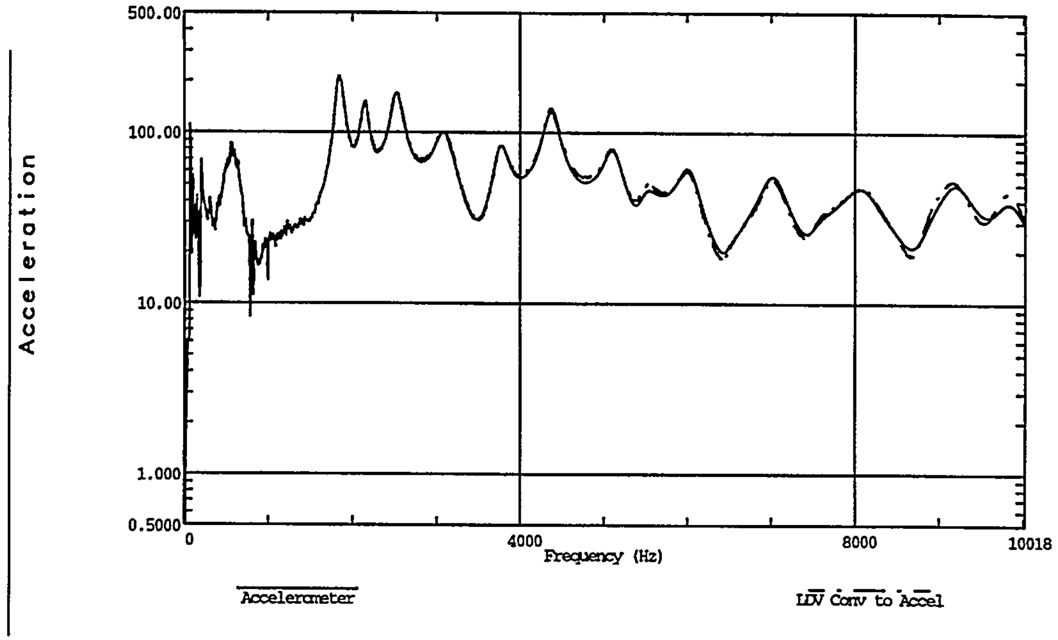

Figure 5.22 Frequency response function comparison, accelerometer -vs- LDV (converted to acceleration)

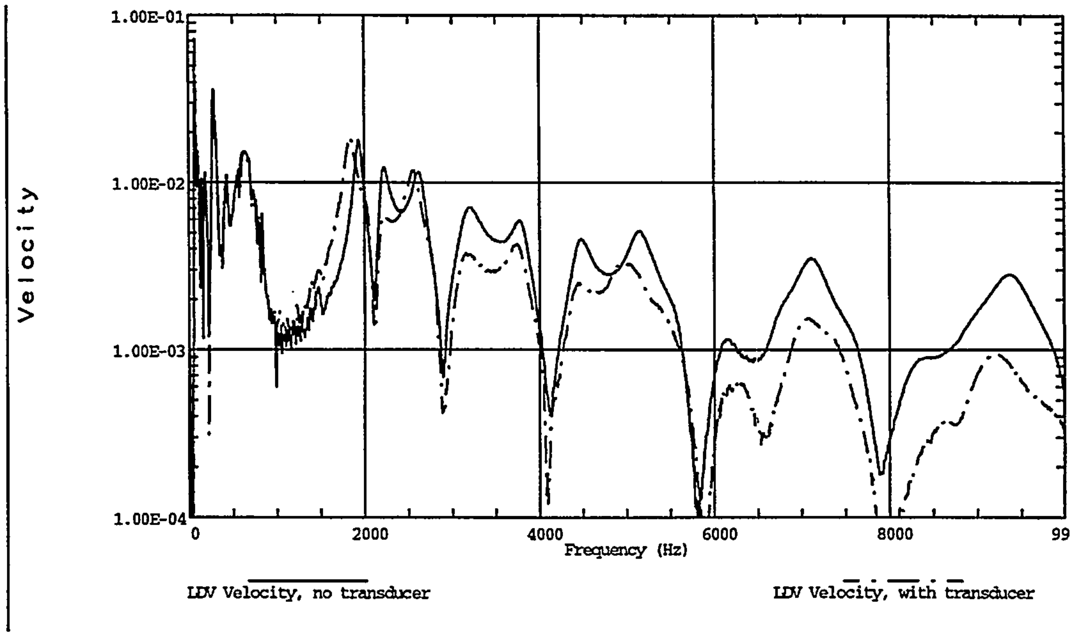

Figure 5.23. Turbine wheel velocity response, with and without single transducer massloading

Chapter 6

Photoelastic Studies

Photoelastic Properties

Excellent discussions of the theory and applications of photoelasticity are given in a number of references [12,13,14,15,16,17] and only the main concepts are discussed here for completeness. The photoelastic properties arise from the fact that many plastics, including epoxies, exhibit birefringence. Birefringent materials are doubly refractive, that is, the refractive index is slightly different in the two planes of propagation of component light rays. Certain transparent materials, notably plastics, are optically isotropic when unstressed but become optically anisotropic when stressed. The change in the index of refraction is a function of the stress applied, similar to the resistivity and the resistance change in a strain gage.

When polarized light travels through a stressed transparent model it is split into two components which vibrate in the two perpendicular planes of principal stress. The velocity of the propagation of each component light ray differs from that in unstressed material by an amount which depends on the magnitude of the stresses. This will result in the time for each light component to travel through the model to be different. Consequently, the two rays emerge from the model out of phase. The difference in phase is proportional to the difference between the two principal stresses, wavelength of the light, thickness of the model, and the stress-optical sensitivity of the material. The two light rays emerging from the model are received by a second polarizer, termed the analyzer, which only transmits the components of the two rays in its plane of polarization. The two emerging components when added together constructively and destructively interfere depending on their relative phase (retardation). Therefore, a variation in magnitude of the principal stress differences at points in the model will cause varying degrees of optical interference resulting in the entire surface of the part appearing to be covered with fringes. Analysis of these fringes allows the differences in principal stresses and strains along with their directions to be determined.

The use of polarized monochromatic (single frequency) light will yield a pattern of light and dark fringes where each dark fringe represents an extinction of the two light ray components when one component is half a wavelength (i.e. 0.5, 1.5, 2.5, etc.) behind the other. Maximum light intensity will create light fringes which occur when one of the components is an integer number of wavelengths behind the other. An example of this is shown in Figures 6.1 and 6.2 for a solid disk and a disk with a center hole made with 5180 epoxy resin subjected to increasing compressive loads. Note the relative number of fringes near the load points and in the vicinity of the hole indicating areas of higher stress.

If polarized white light (contains all frequencies) is used, the model will appear to be covered with a series of brilliantly colored bands, termed isochromatics, having the same color sequence as is observed with a film of oil on water. This effect is due to the varying phase differences (retardations) at different points of the model, which cause each color to be extinguished in turn according to its own wavelength. Every time the retardation is an integer multiple of the wavelength of a particular wave that color disappears and the complementary color is seen. As an example, when the retardation is 25 x 10^{-6} inches (wavelength of the color red) red disappears and green is observed. By selecting the wave length of 22.7 x 10^{-6} inches as a standard wavelength for observation, the full order fringes (N=1,2,3,...) appear between red of the preceding spectrum, and blue or green of the color spectrum following. This can be easily verified by placing a filter (monochromator) such that only the light with a wavelength of 22.7 x 10^{-6} is observed. A dark fringe should occur at each transition of red to blue or green indicating the presence of a full fringe.

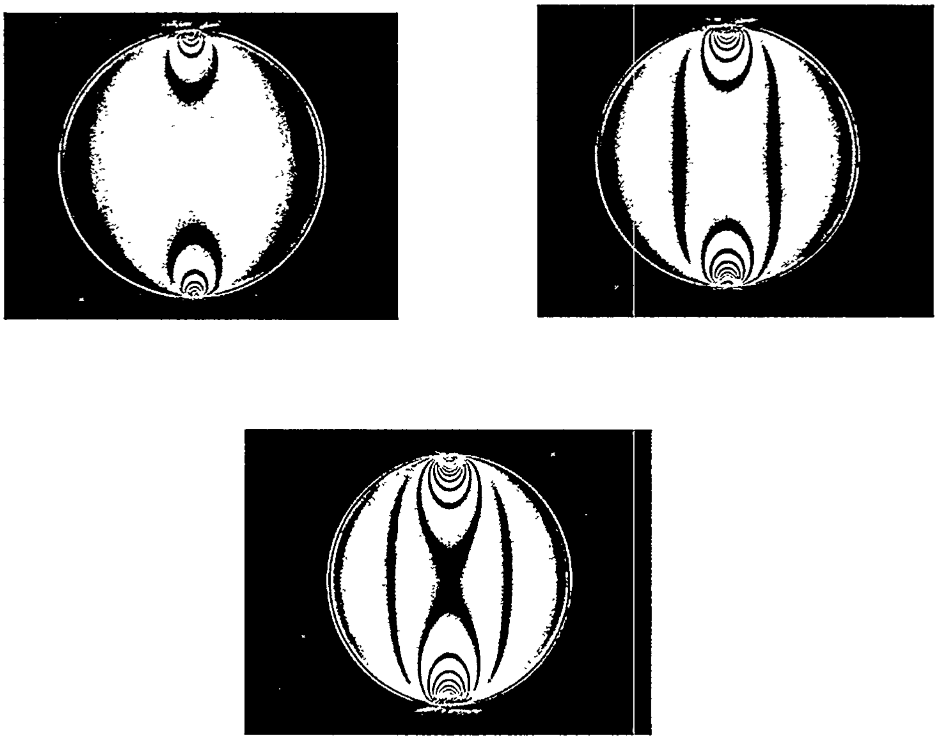

Figure 6.1 Photoelastic fringe patterns of solid 5180 epoxy disk

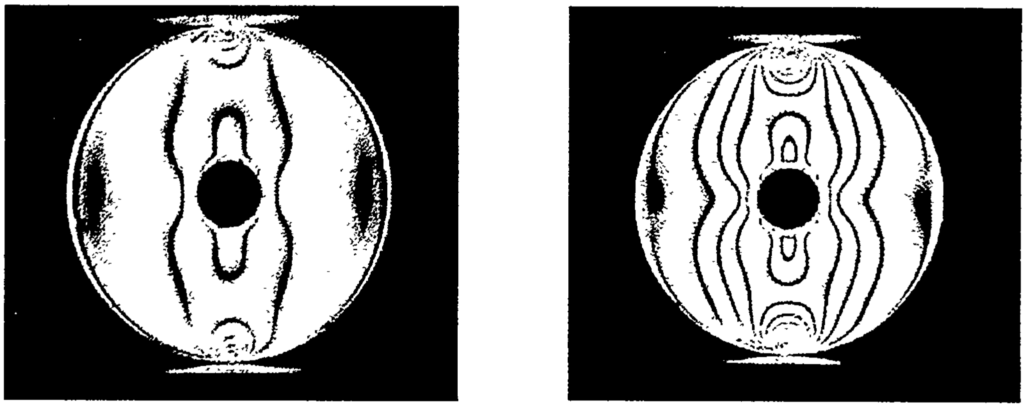

Figure 6.2 Photoelastic fringe patterns of 5180 epoxy disk with hole in center

Stress-Optic Coefficient

The stress and strain in a part (model) can be related to the number of fringes through the stress or strain optic coefficients for the material under study. Various birefringent materials will display different levels of sensitivity to applied loads in terms of the number of fringes for a given stress or strain in the material. The sensitivity and linearity of the 5180 epoxy was investigated to see if this material and resulting prototype parts were candidates for the use of photoelastic stress analysis.

Following the development outlined in Reference [17], the <u>difference</u> in principal stresses, σ_1 and σ_2, in a two-dimensional part can be written as:

$$\sigma_1 - \sigma_2 = 2\tau_{\max} = \frac{C}{b}N \tag{6.1}$$

where σ_1, σ_2 = algebraically maximum and minimum principal stresses, psi

$\tau_{\max}$ = maximum shear stress, psi

C = stress-optic coefficient, psi/fringe/in

b = model thickness, in

N = fringe order, dimensionless

The relationship above is called the stress-optic law and when the stress-optic coefficient, C, and the model thickness, b, are known, the difference between the principal stresses (or the maximum shear stress) is uniquely determined by the observed fringe order at any point in the model. To calculate the stress optic coefficient for a particular lot of material, the above equation is solved for C:

$$C = \frac{b(\sigma_1 - \sigma_2)}{N} = \frac{b(2\tau_{\max})}{N} \tag{6.2}$$

If the thickness and the principal stress difference or the maximum shear stress is known from other considerations or measurements, the stress optic coefficient can be calculated directly from the observed fringe order, N.

The calibration method used in this study to determine the stress-optic coefficient for the 5180 epoxy follows the procedures detailed in Reference [17]. This technique utilizes a standard tensile test specimen which demonstrates a uniaxial stress state in the shank area. This requires that σ_2 equals zero and σ_1 equals the tensile stress in the shank of the specimen. The calibration relationship reduces to

$$C=\frac{b(\sigma_1-\sigma_2)}{N}=\frac{b\sigma}{N} \tag{6.3}$$

For a tensile specimen of width, *h*, and an applied tensile load, *P*, the calibration relationship becomes:

$$C=\frac{b\sigma}{N}=\frac{b}{N}\left(\frac{P}{bh}\right)=\frac{P}{hN} \tag{6.4}$$

The expression for the stress-optic coefficient can also be written in terms of the slope ($\Delta P/\Delta N$) of the relationship between the applied load and the observed fringe order:

$$C=\left(\frac{1}{h}\right)\left(\frac{\Delta P}{\Delta N}\right) \tag{6.5}$$

When the shank of the tensile specimen is observed with a crossed circular polariscope and a monochromatic filter the light intensity in the center of the specimen shank will alternate from minimum (extinction) to maximum to minimum again as the specimen is subjected to increasing loads. The load is increased and the values recorded at each successive fringe are noted through the polariscope. The corresponding loads and fringe orders are then plotted and a best fit straight line is fitted to the data points. The slope of this curve ($\Delta P/\Delta N$) is measured and divided by the shank width, *h*, to yield the stress-optic coefficient, *C*. Note that the magnitude of the stress-optic coefficient, *C*, is a function of the wavelength of light employed. Therefore, if fringe order measurements are to made on the model with monochromatic light, the same monochromator or filter should be used with the model as with the calibration specimen.

"Dogbone" tensile specimens fabricated with 5180 epoxy were used to determine the stress optic coefficient. Holes were made in the ends of each specimen as shown in Figure 2.1 to allow a snug fit with pins in the tensile testing machine. The pins prevent introducing bending into the specimens which would create errors in the measurements. The specimen shank nominal dimensions were 3.0 inches in length, 0.25 inches thick, and 0.325 inches in width. Loads were applied using the tensile test machine over a range of 0 to 400 pounds and a total of twelve fringes were observed. A total of five specimens were tested with two load cycles performed on each specimen. Typical plots for two specimens are shown in Figure 6.3. The computed slopes ($\Delta P/\Delta N$) were divided by the specimen shank width, *h*, to yield the stress-optic coefficients listed on the plots and compiled in Table 6.1. The results are consistent with a slight bias toward the descending values which is probably due to the mechanical creep effects.

The measured values of approximately 195 psi/fringe/in are significantly higher than commercial epoxy photoelastic resins [18] which have stress-optic coefficients at room temperature in the range of 60 - 80 psi/fringe/inch. This results in the 5180 epoxy being one-half to one-third less sensitive than commercial resins tailored for photoelastic stress analysis. The 5180 epoxy will provide fewer fringes for a given stress level than traditional resins used for photoelastic stress analysis. The decreased sensitivity of the 5180 epoxy will not allow quite as dramatic fringe patterns to be visually realized as for commercial photoelastic resins, but partial fringe counting techniques will still allow accurate stress distributions and amplitudes to be computed.

Load Cycle 0 -400 Lbs.	**Specimen 1 psi/fringe/in**	**Specimen 2 psi/fringe/in**	**Specimen 3 psi/fringe/in**	**Specimen 4 psi/fringe/in**	**Specimen 5 psi/fringe/in**
1 - up	184	191	191	190	193
1- down	189	196	195	197	198
2 - up	193	194	194	195	198
2 - down	192	196	196	199	195
Avg.	**191**	**194**	**194**	**195**	**196**

Table 6.1. Stress-optic coefficient measurements for 5180 epoxy tensile specimens

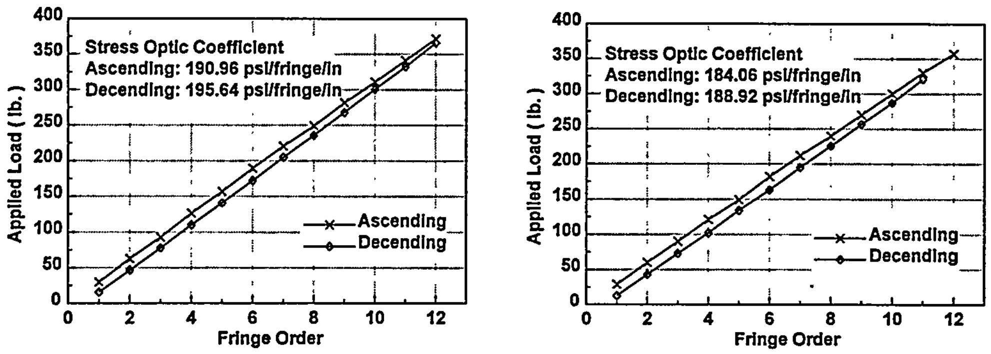

Figure 6.3 Typical stress-optic coefficients for 5180 epoxy

Photoelastic “Frozen Stress” Method

The discussions above apply for two-dimensional techniques for the analysis of stresses occurring in the plane of the model, effectively of uniform thickness. In many design problems the shape of the part is too complicated to permit a useful analysis to be made on a simplified two-dimensional part. A three-dimensional photoelastic analysis of stress in a complicated part can be performed using photoelastic techniques with the “frozen stress” method. In the frozen stress method photoelastic fringes are locked or frozen in position as a result of heat treating a loaded model. Excellent discussions of this powerful technique are provided in References [12,13,15, 17,18]. The main concepts are discussed below.

Materials used for three-dimensional photoelasticity by stress freezing are usually thermosetting polymers that experience a sudden change in mechanical and optical properties above their glass transition temperatures. It is noted in the literature that epoxy resins are some of the best types of plastics available for this technique due to their high optical sensitivity and moduli of elasticity. The technique takes advantage of the multiphase (diphase) nature of plastics to conserve strain and double refraction indefinitely in the model after the loads have been removed. With care, thin slices of material can be cut from the model for analysis without disturbing the frozen-in stress pattern. The analysis can then be carried out on the slices using techniques discussed above for two-dimensional analysis with knowledge of the stress optic coefficient of the material at the stress-freezing temperature. The details associated with determining the principal stresses in the plane of the slice are discussed in the references. The best practices for cutting the slices and enhancing the images with the use of mineral oil are also discussed in the noted references.

The basic procedure used in the stress-freezing involves the following steps:

1. Set up the model in the oven, with the correct loads applied. Some of the references suggest that the loads can be applied after the model has been heated, but this would require handling the model while it is hot. A calibration specimen under a known load should also be placed in the oven along with the model to undergo identical thermal conditioning as the model. The calibration specimen can then be used to determine the stress-optic coefficient of the particular lot of material used to construct the model as discussed later.

2. Heat fairly slowly to a temperature about 10^0F above the softening point of the plastic. (Experiments with the 5180 epoxy show this temperature to be approximately 120^0F to 140^0F). This temperature can be established by observing the on-set of fringe lines in the model or calibration specimen by detecting the emergence of fringes through the use of a transparent window and polarized light source.

times are one hour for thin sections and small models, and up to six hours for large masses)

4. Cool to room temperature at a slow and uniform rate, so that thermal stresses are avoided. Very conservative cooling rates should be used. (Suggested rates are 2-5^{0}F/hour for thick sections and 10^{0}F/hour for thin sections)

The key question to be answered in this study was if the 5180 epoxy used in the stereolithography process had the sufficient properties to allow application of the "frozen stress" technique for three-dimensional stress analysis. The issue of the layering technique utilized in the stereolithography process and the use of photoreactive resins in the process were investigated. Calibration specimens were fabricated from the 5180 epoxy resins with the material lay up oriented in the plane and normal to the plane of the specimen. The procedures defined in Reference [17] were followed with the theory and main concepts repeated here for completeness.

Convenient specimens for the calibration of models are simply supported beams in pure bending as shown in Figure 6.4. When loaded as shown in the figure the bending moment is constant over the span l_2, and near the center of l_2 (away from the points of load application) the stress state is <u>uniaxial</u> and independent of position along the beam axis. The axial stress in this region at distance y, from the neutral axis is:

$$\sigma_x(y) = \frac{My}{I} = \frac{(P/2)l_1 y}{bh^3/12} = \frac{6Pl_1 y}{bh^3} \tag{6.6}$$

where:

$\sigma_x(y)$ = axial stress as a function of y, psi
y = distance from the neutral axis of beam, in
M = bending moment over span, l_2, in-lb
I = moment of inertial of beam cross section, in^4
P = applied load, lb
b = thickness of calibration beam, in
h = width of calibration beam, in

Using the stress-optic law, noting that in the central portion of the beam there is only one non-zero principal stress, the stress -optic law becomes:

$$\sigma_1(y) - \sigma_2(y) = |\sigma_x(y)| = \frac{C}{b} N(y) \tag{6.7}$$

where:

$\sigma_1(y)$, $\sigma_2(y)$ = algebraically maximum and minimum principal stress as functions of, y, psi

$|\sigma_x(y)|$ = absolute value of the axial stress, since N must be positive, psi
N(y) = fringe order as a function of y

Combining the above two equations and solving for the stress-optic coefficient yields:

$$C = \frac{6Pl_1}{h^3}\left(\frac{|y|}{N(y)}\right) \tag{6.8}$$

where: $|y|$ = absolute value of y

Plotting N(y) versus y′ (the coordinate from the top or bottom of the beam) the slope of the curve $\Delta|y|/\Delta N(y)$ can be obtained for substitution into Equation (6.8). The most accurate value of the slope can be obtained by fitting a straight line through the data and extrapolating the line to the boundaries. The beam depth divided by the sum of the fringe orders at the two boundaries gives the required slope for substitution into Equation (6.9). This gives:

$$C = \frac{6Pl_1}{h^3}\left(\frac{h}{N_U + N_L}\right) \tag{6.9}$$

where:

N_U, N_L = extrapolated fringe order at upper and lower beam boundaries, respectively

Calibration beams were fabricated with the stereolithography process using the 5180 epoxy resins with material lay-up oriented in different directions to evaluate any effects of the material build axis. The X-Flat and Y-Flat beams had the material build axis in the plane of the beams. The X-Edge and Y-Edge beams were fabricated with the material build axis normal to the plane of the beams. The beams were placed in a special loading frame supplied in a the Model 041 Calibration Kit by Measurements Group Inc. Calibrations were performed with both a 5.0 lb and a 10.0 lb weight suspended from the loading frame. Two specimens were tested at one time with the effective weight (including pins and other hardware) acting on each beam carefully measured. The beams were placed in an oven and the temperature slowly increased while observing for indications of the initiation of fringes. During this study the first indication of fringes were observed at approximately 130^0 F. The oven temperature was increased to 200^0 F and maintained for two hours and slowly decreased back to ambient temperature at a rate of 5^0 F per hour. Photographs of the frozen stress fringes in the beams using monochromatic light are shown in Figures 6.5 and 6.6 for the 5.0 and 10.0 pound loadings, respectively.

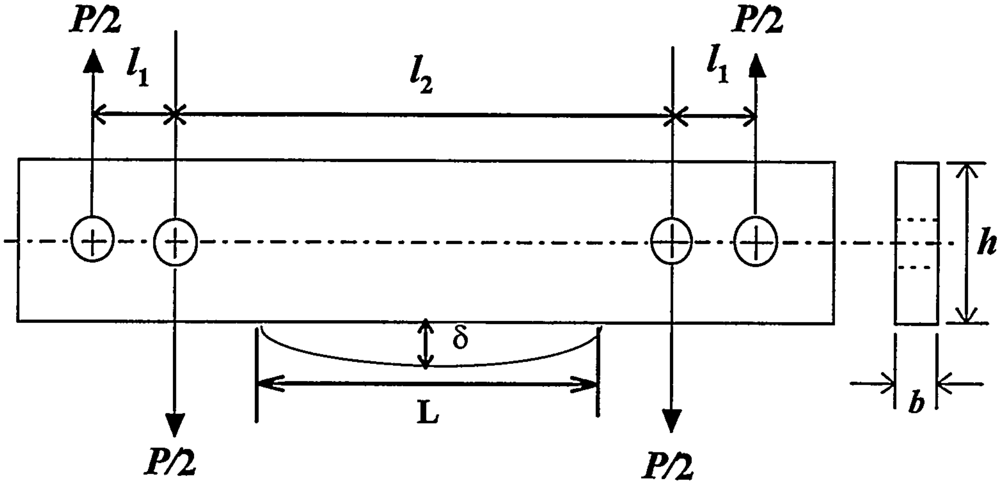

Figure 6.4 Calibration beam for stress-optic coefficient at stress freezing temp.

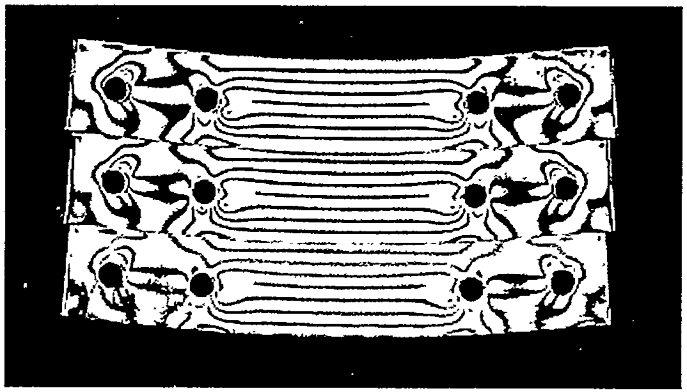

Figure 6.5 Stress freezing calibration with 5.0 lb load

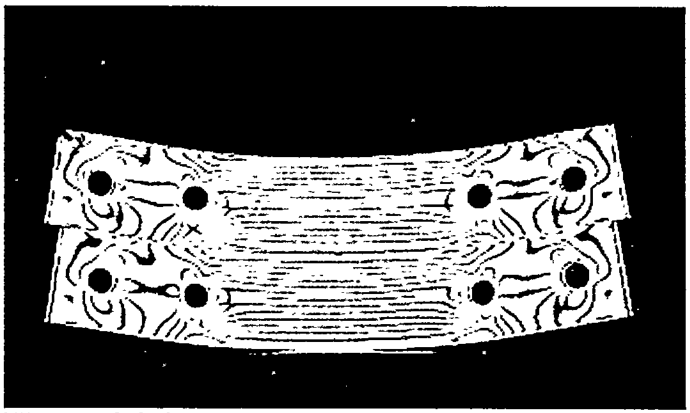

Figure 6.6 Stress freezing calibration with 10.0 lb load

The stress optic coefficients were determined using Equation (6.9). The fringes and fringe spacings were measured using a Model 060 Transmission Polariscope with a telemicroscope supplied by Measurements Group Inc. Plots for typical calibrations for two levels of loading are shown in Figures 6.7 - 6.9. The results for all of the calibrations are given in Table 6.2. The stress-optic coefficients were consistent for the different material lay-up directions and loading levels indicating linearity with level and material lay-up orientation. The average stress-optic coefficient at the stress freezing temperature measured for the 5180 epoxy was approximately 4.3 psi/fringe/inch. The commercial epoxy resins tailored for stress freezing have stress-optic coefficients in the range of 2.0 to 2.5 psi/fringe/inch, which are approximately one-half that measured for the 5180 epoxy. This result indicates that for a given level of stress in the part the 5180 epoxy will have approximately one-half the number of fringes that the commercial epoxy resins would provide.

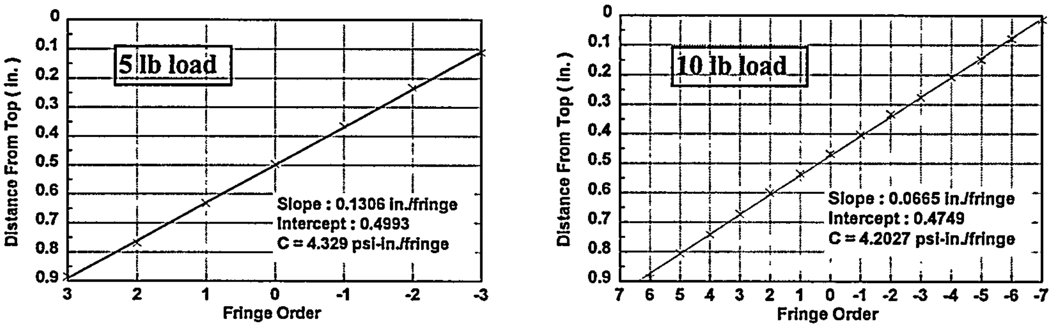

Figure 6.7 Stress-optic coefficient in Y-flat direction with 5.0 and 10.0 lb load

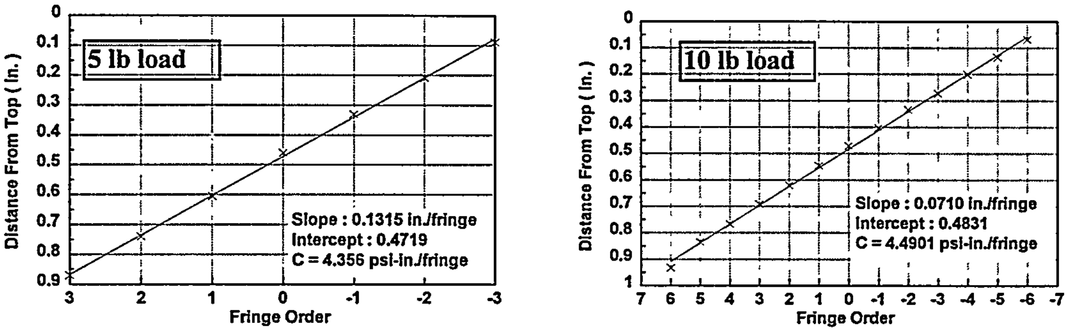

Figure 6.8 Stress-optic coefficient in Y-edge direction with 5 and 10 lb load

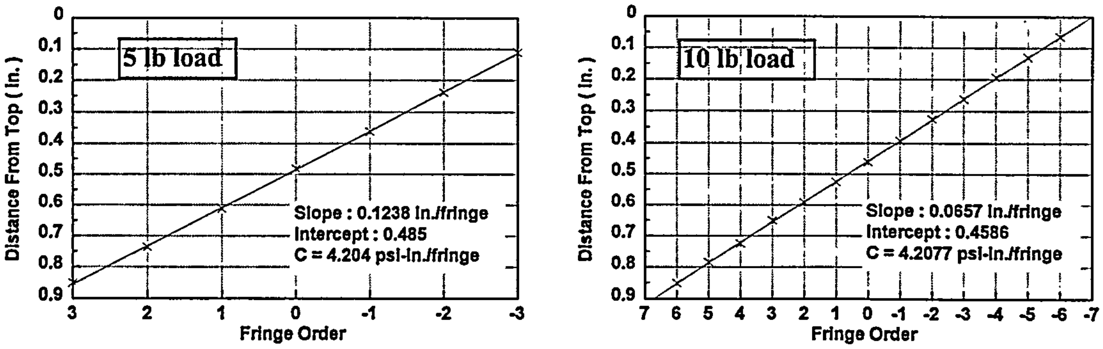

Figure 6.9. Stress-optic coefficient in X-flat direction with 5.0 and 10.0 lb load

Material Lay-up Direction (X and Y Axes are in Plane of Lay-up, Z axis is Normal to Plane of Lay-up)	**Stress-Optic Coefficient at Stress Freezing Temperature w/ 5.0 lb Load** (psi /fringe/inch)	**Stress-Optic Coefficient at Stress Freezing Temperature w/10.0 lb Load** (psi /fringe/inch)
Y - Flat (No. 1)	4.329	4.203
Y- Flat (No. 2)	4.233	No Data
X - Flat	4.204	4.208
Y - Edge (Z - Axis)	4.356	4.490
X - Edge (Z - Axis)	No Data	4.289
Avg.	**4.281**	**4.298**

Table 6.2 5180 epoxy stress-optic coefficient at stress freezing temperature

Since the central portion of the calibration beam is subjected to a uniform bending moment the deflection curve in this region takes the form of a circular arc. Knowing the bending moment and cross-sectional dimensions, the elastic modulus can be estimated from the radius of curvature of the arc. The radius of curvature can be expressed in terms of the arc height over a predetermined span or chord. With some simplifying assumptions as discussed in Reference [17], the elastic modulus at the stress freezing temperature can be estimated by:

$$E = \frac{3l_1PL^2}{4bh^3\delta} \tag{6.10}$$

where:

δ = arc height measured over the chord length L, in
L = chord length used to measure the arc height, δ, in

The arc height, δ, and associated chord length, L, to calculate the elastic modulus from the calibration beams are shown in Figure 6.4. These measurements were taken using a specially designed dial indicator supplied in the Model 401 Calibration Kit from Measurements Group Inc. The measured results were used with Equation (6.10) to calculate the elastic modulus at the stress freezing temperature for the 5180 epoxy calibration beams. The results are summarized in Table 6.3. The measured elastic modulus for the 5180 show fairly consistent results with the elastic modulus measured at the 10.0 lb load showing slightly higher values. No appreciable differences were found for the various material lay-up directions. These results correlate well the elastic modulus of approximately 2000 - 2500 psi for commercial epoxy resins used for stress freezing experiments.

Material Lay-up Direction (X and Y Axes are in Plane of Lay-up, Z axis is Normal to Plane of Lay-up)	**Elastic Modulus at Stress Freezing Temperature w/ 5.0 lb Load (psi)**	**Elastic Modulus at Stress Freezing Temperature w/10.0 lb Load (psi)**
Y - Flat (No. 1)	2218	2400
Y- Flat (No. 2)	2165	No Data
X - Flat	2137	2291
Y - Edge (Z - Axis)	2191	2344
X - Edge (Z - Axis)	No Data	2365
Avg.	**2178**	**2350**

Table 6.3 Elastic modulus of 5180 epoxy at stress freezing temperature

Chapter 7

Conclusions

A number of experiments were performed to evaluate the ability to predict structural behavior of metal parts from the measured behavior of plastic prototype parts generated with the stereolithography process. The integration of advanced non-contacting measurement techniques including laser Doppler velocimetry, holography, thermoelasticity, and photoelasticity into the testing of stereolithography plastic parts was also demonstrated.

Material characterization tests indicate the 5170 and 5180 epoxies are superior to the 5154 acrylic resin for the purposes of this study (predict metal performance) due to their higher elastic moduli and dimensional stability. The results further indicate that the epoxy resins are isotropic with the elastic moduli independent of direction.

One of the most accurate uses of the plastic prototype parts is the prediction of natural (modal) frequencies of metal parts. The scaling of plastic frequencies is slightly complicated by the fact that the epoxy resins are strain rate sensitive and possess elastic moduli which are functions of frequency. Accurate scaling of natural frequencies of the plastic parts to those of metal parts requires the elastic modulus of the epoxy be measured as a function of frequency. Simple experiments on calibration beams can be used to determine the elastic modulus as a function of frequency. Frequency scaling errors of approximately 5% should be anticipated if the dynamic modulus is carefully measured from the same lot of material as the plastic prototype part. Care must also be exercised to prevent mass-loading effects from mounted transducers which will create errors for the light weight plastic prototypes. The use of non-contacting measurement techniques such as laser Doppler velocimetry and holographic techniques can eliminate this problem. For practical purposes, a scaling factor of approximately 3.0 (metal frequency ≈ 3.0 * plastic frequency) will provide reasonably accurate results for steel, aluminum, magnesium, and titanium.

Mode shapes were found to compare closely between the metal and plastic parts indicating the that the relative displacement patterns associated with each natural frequency are similar. The effects of mass loading due to attached transducers also needs to be considered when predicting mode shapes. The results in this study for the fire-set covers showed less sensitivity to the mass loading for the mode shapes than for the modal frequencies which were significantly changed with the attachment of 52 accelerometers. The principal of reciprocity allows the use of fewer attached transducers with the impact location of the instrumented hammer to be made at multiple points vs. many accelerometers which may be the preferred means of conducting a modal survey to obtain the frequencies and mode shapes of plastic parts.

The damping of the plastic prototype parts was found (as expected) to be much higher than for the metal parts. The experiments, however, did not reveal a clear means of scaling the damping since the damping values determined from the modal tests varied from mode to mode in an inconsistent manner in the plastic parts as well as the metal parts. For the purpose of order of magnitude comparisons a ratio of steel to plastic damping of approximately 0.04 is suggested. Further research is required under more controlled boundary conditions (eliminate interaction with foam supports) to more clearly understand the relationship of damping in the plastic and metal parts.

The ESPI system demonstrated the ability to provide real time, full field, operating shapes for the vibrational behavior of both plastic and metal parts. Excellent correlation of the operating shapes were found for the bicycle crank and turbine wheels which possessed widely spaced modal frequencies. The operating shapes for the metal and plastic fire-set covers were not as similar due to effects of the increased damping of the plastic parts with closely spaced modal frequencies. The operating shapes are found by applying sinusoidal excitation to the structure at a single frequency and observing the response via the resulting fringe pattern. The increased damping creates greater coupling between adjacent structural modes than for the equivalent metal structure. Therefore, the plastic operating shapes contain greater contributions of adjacent modes and the resulting images will show differences from the metal parts. However, the principal vibration mode at the excitation frequency will still dominate the response allowing correlation of relative displacements in the parts for design purposes. The effects of the physical attachment of a shaker to the prototype parts needs to be carefully examined for each experiment since the local stiffening and mass loading effects of the shaker can also create errors. The use of non-contacting excitation such as acoustic, demonstrated for the fireset cover study, can help eliminate these affects.

The epoxy resins, as do most other plastics, undergo mechanical creep when subjected to sustained static loads. The results of the experiments show that the creep rate increases with the load (stress) in the plastic part. The creep experiments performed indicate that creep rates are not excessive, but will create errors when making static stress and deflection measurements to predict actual metal part performance. Care must be taken to properly scale loads in the plastic part (as low as possible) and to perform measurements in a timely manner.

The prediction of static deflections, strains, and stresses of metal parts from plastic prototype parts revealed some complications. The plastic parts often have internal residual stresses due to the selective curing process used in stereolithography. These residual stresses can create errors which typically become smaller for increasing stress levels. Preliminary results indicate that annealing of the plastic parts at slightly elevated temperatures may provide some improvement for this effect. The flexibilities of the fixtures and load application equipment must also be accounted for, particularly for testing metal parts, when comparing the static test results between plastic and metal parts. The precise positioning and orientation of strain gages are critical, particularly in areas of high strain gradient, in the measurement of strain using traditional strain gages. Considering all the sources of error, including mechanical creep, scaling errors of approximately 20% can be expected in predicting point strain measurements with traditional strain gages. The strain distributions showed good correlation between the metal and plastic parts which are often as valuable to the designer and structural analyst as the absolute values of the strain.

The ESPI system also showed great utility and enhanced measurement capability for the measurement of real time, full field deflection patterns in both plastic and metal prototype parts under static loads. The ESPI system allows the detailed deflection distribution to be observed as a fringe pattern superimposed on the actual structure. This imaging technique can provide unique insight to the designer of where and how the deflections (strains/stresses) are realized in the prototype part. The use of the COBRA code with the finite element model results showed excellent correlation for the bicycle crank. This technique provides a means for direct correlation of the experimental and analytical results for model optimization and validation for the full field displacement patterns.

The uses of thermoelastic imaging to predict full field stress patterns was successfully demonstrated for a stereolithography prototype part. This technology also provides the means of providing quantitative stress measurements once the thermoelastic constants are determined from simple material calibrations or by comparison with a strain gage mounted on the structure.

The epoxy resins were found to have photoelastic properties allowing the full field stress/strain behavior of the plastic prototype parts to be measured. Experiments show that the stress-optical sensitivity (number of fringes for a given level of stress) of the epoxy resins are approximately one-half to one-third the sensitivity of commercial photoelastic epoxy resins specifically designed for stress analysis. Stress freezing experiments show that the epoxy resins do indeed have the properties to allow three-dimensional stress analysis using the frozen-stress technique.

In summary, the 5170 and 5180 stereolithography prototype parts can be used to predict metal part structural behavior including: stress/strain, deflections, modal frequencies, mode shapes, and operating shapes with some limitations. Mechanical creep effects must be considered when making static measurements of stress/ strain and deflections. Methods for scaling damping from plastic to metal were not found, and the increased damping creates errors for closely spaced modal frequencies in the operating shapes as measured by the ESPI system.

References

[1] Jacobs, P. F., Rapid Prototyping & Manufacturing Fundamentals of StereoLithography, McGraw, 1992.

[2] Baker, W. E., Westine, P.S, and Dodge, F. T., Similarity Methods in Engineering Dynamics, Hayden Book Co. Inc., 1973

[3] Wright, D. V. and Bannister, R. C., "Plastic Models for Structural Analysis", Part I; Testing Types, Shock & Vibration Digest, Volume 2, No. 11, Nov. 1970, pp 2-10.

[4] Sankey, G. O., "Plastic Models for Vibration Analysis", Proceedings SESA, XI, No. 2, pp 81-90, 1954.

[5] Parks, Vincent J., Geometric Moiré, *Handbook on Experimental Mechanics*, Kobayashi, A. S. ed., Chapter 6, Society for Experimental Mechanics, 1993.

[6] Vest, C. M., Holographic Interferometry, John Wiley & Sons, New York, 1979.

[7] Ranson, W. F., Sutton, M. A. and Peters, W. H. Holographic and Laser Speckle Interferometry, *Handbook on Experimental Mechanics,* Chapter 8, Kobayashi A. S. ed., Society for Experimental Mechanics, 1993.

[8] Drain, L. E., The Laser Doppler Technique, John Wiley & Sons, New York, 1980.

[9] Rauch, B. J. and Rowlands, R. E., Thermoelastic Stress Analysis, *Handbook on Experimental Mechanics,* Chapter 14, Kobayashi A. S. ed., Society for Experimental Mechanics, 1993.

[10] Nielsen, L. E., Mechanical Properties of Polymers, Reinhold Publishing Corp., 1962

[11] Volterra, E. and Zachmanoglou E. C., Dynamics of Vibrations, Charles E Merrill Books, Inc., Ohio, 1965.

[12] Kuske, A. and Robertson, G., Photoelastic Stress Analysis, John Wiley and Sons Ltd, 1974.

[13] Heywood, R. B., Photoelasticity for Designers, Pergamon Press Ltd., London England, 1969.

[14] Redner, "Model Approach in Structural Design", Meeting Preprint 2205, ASCE National Structural Engineering Meeting, Cincinnati, OH, April, 22-26, 1974.

[15] Frocht, M. M., Photoelasticity, Volume 1, John Wiley & Sons Ltd, 1962.

[16] Measurements Group Inc., "Introduction to Stress Analysis by the PhotoStress Method", Technical Note TN-702, 1981.

[17] Measurements Group Inc., "Calibration of Photoelastic Plastics for Two - and Three - Dimensional Model Analysis", Technical Note TN - 705, 1982.

[18] Measurements Group Inc., "Model Making for Three - Dimensional Photoelastic Stress Analysis", Technical Note TN - 707, 1982.

DISTRIBUTION:

1 Jay Steidle
3D Systems
9574 Whippoorwill Lane
Mason, OH 45040

1 Kevin Dalton
Aircraft Braking Systems Corp.
Dept. 693 B2
1204 Massillon
Akron, OH 44306

1 Sterling Franks, III, Associate Director
Office of Engineering and Technology Development
U. S. Department of Energy
19901 Germantown Road
Germantown, MD 20874

1 Dennis Harrison, Program Director
Commercial Operating LWR Program
Office of Engineering and Technology Development (NE-50)
U.S. Department of Energy
19901 Germantown Road
Germantown, MD 20874

1 Dr. Hans Mark
Professor and John J. Mcketta
Centennial Energy Chair in Engineering
Department of Aerospace Engineering, and Engineering Mechanics
University of Texas at Austin
Austin, TX 78712

1 Bob Carman
Rockwell/Rocketdyne
P. O. 7922
Canoga Park, CA 91309

1 Martin J. Pechersky
Savannah River Technology Center
Westinghouse Savannah River Company
Building 773-A
Aiken, SC 29808

DISTRIBUTION (cont.):

1 Dr. Wen Jeng Chen
Ingersoll - Rand
Centrifugal Compressor Division
Highway 45 South
Mayfield, KY 42066

1 Clint Logan
Lawrence Livermore National Laboratory
Mail Stop L-333
PO Box 808
Livermore CA 94550

1	0960	J. Q. Searcy, 1400
1	0958	J. W. Munford, 1484
5	0958	C. L. Atwood, 1484
1	0958	B. T. Pardo, 1484-1
1	0958	D. E. Reckaway, 1484-1
1	9405	D. L. Lindner, 1809
1	0955	W. E. Alzheimer, 1900
1	0429	R. D. Andreas, 2100
1	0481	R. G. Bell, 2167
1	0509	W. D. Williams, 2300
1	0505	D. L. Eilers, 2336
1	1436	LDRD office, 4523
1	0458	J. S. Rottler, 5139
1	9403	B. Fuchs, 8712
1	0151	G. Yonas, 9000
1	0819	J. M. McGlaun, 9231
1	0820	P. Yarrington, 9232
1	0439	D. R. Martinez, 9234
1	0439	G. M. Reese, 9234
1	0949	R. W. Harrigan, 9602
1	1006	P. Garcia, 9671
1	0507	K. G. McCaughey, 9700
1	0555	R. A. May, 9706
1	0555	D. B. Davis, 9732
1	0865	J. L. Moya, 9735
1	0557	W. N. Dunn, 9735
1	0557	J. S. Cap, 9735
1	0557	D. O. Smallwood, 9735
1	0557	T. J. Baca, 9741
1	0557	S. E. Klenke, 9741

DISTRIBUTION (cont.):

1	0557	J. P. Lauffer, 9741
1	0557	T. G. Carne, 9741
1	0557	T. L. Paez, 9741
1	0557	P. S. Barney, 9741
1	0557	R. L. Mayes, 9741
10	0555	M. S. Garrett, 9742
20	0555	D. L. Gregory, 9742
20	0555	B. D. Hansche, 9742
1	0555	T. C. Togami, 9742
1	0615	W. W. Shurtleff, 9752
1	0615	M. Valley, 9752
1	0555	M. E. F. Shields, 9752
1	1135	J. R. Garcia, 9761
1	0163	J. Polito, 9800
1	0163	D. M. Rondeau, 9803
1	9018	Central Technical Files, 8523-2
5	0899	Technical Library, 4414
1	0619	Print Media, 12615
2	0100	Document Processing, 7613-2 for DOE/OSTI